ELECTROCHEMISTRY

Alcohol molecule coupling: A universal approach to modulating amorphousness in vanadium-based cathodes for high-rate and durable aqueous zinc-ion batteries

Haobin Song[1]†, Yang-feng Cui[1]†, Yifan Li[1], Xueliang Li[1], Yixiang Li[1], Nan Zhao[1], Wenjing Li[1], Chao Wu[2], Shibo Xi[2], Shaozhuan Huang[3], Hui Ying Yang[1]*

Vanadium oxides (VOs) are promising cathode materials for aqueous batteries due to their high theoretical capacity, but they face challenges such as sluggish kinetics and V dissolution. To overcome these issues, we introduce a universal alcohol-based molecule coupling (AMC) method to regulate amorphousness and inhibit V dissolution in VOs (VO_2, V_2O_5, and V_6O_{13}), resulting in high-performance cathodes. The strategy enables alcohol molecules with different chain lengths (ethanol, isopropanol, and isobutanol) to couple with VOs by forming V—OH bonds under Lewis acid–based interactions, inducing controlled amorphization. Among these, isopropanol coupling stands out by enabling the formation of short-range ordered amorphous structure (SOA-VO/Ipr). This structure enhances the reaction kinetics and suppresses V dissolution. As a result, the SOA-VO/Ipr cathode achieves 219.4 mAh g^{-1} at 100 A g^{-1}, retains 92.6% capacity over 10,000 cycles, and delivers 228.8 mAh g^{-1} at 9.1 A g^{-1} under high loading (21.9 mg cm^{-2}) over 3500 cycles, demonstrating a promising method for durable zinc-ion batteries.

INTRODUCTION

Aqueous zinc-ion batteries (AZIBs) are emerging as a highly promising system for next-generation large-scale energy storage applications due to their enhanced safety, cost-effectiveness, and impressive specific capacity of zinc metal (820 mAh g^{-1}) (*1*). However, the larger ion radius of Zn^{2+} (0.74 Å) and the involvement of two electrons in the reaction result in suboptimal kinetics of the cathode, hindering fast charging and extended cycle life (*2*). Therefore, identifying suitable cathode materials is crucial to overcoming these challenges (*3*). Commonly considered options include manganese-based oxides (*4*), vanadium-based oxides (VOs) (*5*), Prussian blue (*6*), and organic materials (*7*). Among them, VOs are garnering increasing attention due to their high theoretical specific capacity (typically >300 mAh g^{-1}) and abundant resource. However, the sluggish reaction kinetics of crystalline VOs and the dissolution of V in aqueous electrolytes severely hinder the development of V-based cathodes (*8*).

Recently, various strategies, including amorphous structure design (*9*), guest species incorporation (*10*), defect engineering (*11*), and surface modification (*12*), have been proposed to address the challenges faced by V-based cathodes. Among them, amorphous structure engineering has proven to be effective in enhancing the reaction kinetics of V-based cathodes because the disordered atom arrangement of amorphous structures could shorten the zinc-ion transport pathways and mitigate the lattice expansion upon the zinc-ion intercalation/deintercalation (*9*, *13*). However, the amorphous VOs are prone to more serious V dissolution in comparison to crystalline VOs due to the less stable structure and higher entropy of amorphous VOs (*14*–*16*). To thermodynamically inhibit the V dissolution, introducing guest species into V_2O_5 layers is an effective method because guest species incorporation could stabilize the bulk structure (*17*) by forming coordinate bonds, thereby resisting H_2O attack and reducing V solubility. For instance, Xia and colleagues (*18*) reported a layered $NH_4V_3O_8$ aqueous cathode intercalated with a polymer (PEDOT), which achieved an exceptional capacity retention of 94.1% after 5000 cycles. This molecule-level coupling within layered V-based cathodes effectively maximizes the protection of V atoms from H_2O-induced degradation, thus enabling stable long-term cycling performance. Nevertheless, the guest species incorporation is usually based on the crystalline V_2O_5, which still suffers from sluggish reaction kinetics (*19*, *20*). Therefore, combining amorphous structure engineering and guest species incorporation could yield a synergistic effect, which may simultaneously inhibit the V dissolution and enhance the reaction kinetics. However, to date, there have been few reports on this specific structure.

In this study, we introduce a universal alcohol-based molecule coupling (AMC) method that can precisely regulate the amorphous degree of various VOs, including VO_2, V_2O_5, and V_6O_{13}. Taking V_2O_5 (theoretical specific capacity, ~589.4 mAh g^{-1}) as a model system, we demonstrate that alcohol molecules of varying chain lengths [ethanol (Et), isopropanol (Ipr), and isobutanol (Ibu)] can well tune the crystal structure and couple with V_2O_5 at the atomic scale. The reductive properties of these alcohol molecules facilitate the breakage of original V—O bonds, while the varying chain lengths of the molecules enable precise tuning of the V_2O_5 structure from crystalline to short-range ordered amorphous to fully disordered amorphous. Initially, the V atoms in V_2O_5 are reduced by these reductive agents and subsequently coupled with the alcohol molecules through a Lewis acid–based hydroxy-V (—OH—V) interaction. During this coupling process, the medium chain length of Ipr distorts the V_2O_5 crystal planes and partially disrupts the crystalline structure, resulting in a moderately short-range ordered amorphous structure

(SOA-VO/Ipr). The Ipr coupling effectively stabilizes the amorphous structure and suppresses the hydrolysis reaction of V_2O_5, thereby slowing the spontaneous V dissolution process. Density functional theory (DFT) calculations present a positive bonding energy between H_2O and SOA-VO/Ipr, confirming the great difficulty of chemical bonding between SOA-VO/Ipr and H_2O molecule. This result demonstrates that SOA-VO/Ipr exhibits excellent resistance to hydrolysis, effectively preventing the degradation of V_2O_5 and subsequent V dissolution. Furthermore, the Ipr-induced short-range ordered amorphous structure reinforces the amorphous network, providing more channels for Zn^{2+} transport, thereby enhancing the reaction kinetics. Consequently, the SOA-VO/Ipr cathode exhibits remarkable performance in zinc-ion batteries, achieving a high specific capacity of 219.4 mAh g^{-1} at an ultrahigh current density of 100 A g^{-1} and ultralong cycle life over 10,000 cycles at 30 A g^{-1}. Similarly, the AMC method is well suited for other types of VOs (VO_2, V_6O_{13}, etc.), enabling the controllable regulation of amorphousness and the realization of high-performance AZIB. Furthermore, the proposed SOA-VO/Ipr cathode demonstrated outstanding practical performance, meeting the requirements of high-loading cathodes. Even at the loadings exceeding 20 mg cm^{-2}, the cathode still exhibits stable cycling under both low current density (0.2 A g^{-1} for 100 cycles with an impressive discharge specific capacity of 395 mAh g^{-1}) and high current density conditions (9.1 A g^{-1} for 3500 cycles with a notable discharge specific capacity of 228.8 mAh g^{-1}). These compelling results underscore the practicability of the universal AMC method in advancing high-energy, durable AZIB.

RESULTS

Synthetic routine and mechanism analysis

Organic molecules containing hydroxyl groups (alcohol-based molecules) exhibit reducibility because the oxygen atom in —OH serves as an electron donor (*21*, *22*), participating in redox reactions with electron acceptor materials (EAMs) such as manganese oxides (*23*), iron oxides (*24*), and VOs (*25*). In this process, alcohol molecules tightly coupled with the EAMs at the atomic scale, influencing their crystalline structure through the length of their molecular chains. Specifically, alcohol-based molecules initially reduce the EAMs, leading to an imbalance in the electron state of the EAMs. Subsequently, the electron-donating —OH group in these molecules interacts with the EAMs through Lewis acid–based interactions. This interaction leads to the formation of bonds between alcohol-based molecules and EAMs. Because of their varying molecular chain lengths, the EAMs exhibit distinct atomic arrangements with varying degrees of amorphousness. Taking V_2O_5 as an example, three types of alcohol molecules, Et, Ipr, and Ibu, were used as electron donors to modulate the degree of amorphousness (Fig. 1). These alcohol molecules donate electrons to the V atoms, partially filling the vacant outer orbitals of V^{5+}, thereby enabling V to couple with the —OH groups (Fig. 1A). The coupling strength correlates with the electron-donating capability of the —OH group, while the crystalline structure adapts to the chain length of the alcohol molecules (Fig. 1B). The small Et molecules merely insert into the layers of V_2O_5 without noticeable changes in the crystal structure (VO/Et; theoretical specific capacity, ~509.8 mAh g^{-1}) (*26*). In contrast, the Ipr molecules with moderate chain length cause crystal plane distortion and partially destruct the crystal structure, forming a short-range ordered amorphous structure (SOA-VO/Ipr: theoretical specific

capacity, ~512.9 mAh g^{-1}). Furthermore, the Ibu molecules with longer chain length induce severe crystal disruption, resulting in a fully disordered amorphous structure (FDA-VO/Ibu; theoretical specific capacity, ~501 mAh g^{-1}).

To further elucidate the coupling process and directly observe the modulation mechanisms described above, we used a series of characterization techniques. First, under ultrasonication, the V_2O_5 layers were exfoliated into smaller fragments (fig. S1). Second, thermal treatment facilitated the reaction between V_2O_5 and the alcohol solvent, leading to the partial reduction of V^{5+} to V^{4+} in V_2O_5 (fig. S2) and oxidation of —OH groups to —C=O (*27*, *28*). Subsequently, Et, Ipr, and Ibu molecules are coupled with V_2O_5 through —OH interacting with V atoms (*27*), which disrupt the original V—O bonds and form new V—OH coordinate bonds. During solvent evaporation, lower-boiling aldehyde, ketone, and unreacted alcohol molecules are evaporated, while the coupled alcohol molecules remain within V_2O_5 due to the bonding effect. The representative color change during the synthesis of SOA-VO/Ipr is illustrated in fig. S3. Upon heating, the solution color shifts to pale yellow (fig. S3, A to C), corresponding to the reduction of V^{5+} to V^{4+} by Ipr. After coupling with Ipr, the color of V_2O_5 changes to black (fig. S3D). Similar transformations were observed in the Et and Ibu coupling reactions (fig. S4). To observe the modulation process, we used x-ray diffraction (XRD), transmission electron microscopy (TEM), high-resolution TEM (HRTEM), and selected-area electron diffraction (SAED) to study the morphology and structure of V_2O_5. As shown in Fig. 2 (A to E) and fig. S5, the commercial V_2O_5 shows a typical crystalline structure with a single-layered structure (PDF#01-085-0601; Fig. 2, A and E, and fig. S5A). After coupling with Et molecules, the crystallinity of V_2O_5 is notably weakened because of the structural disordering, while part of VO/Et still maintains the crystalline structure, as confirmed by the SAED and XRD patterns (Fig. 2, B and E). The appearance of broad peaks at 26.2° and 50.4° suggests the formation of amorphous domain. The HRTEM image further reveals the disordered lattice fringes, confirming the poor degree of crystallinity. When coupled with Ipr, the peaks representing the crystalline V_2O_5 nearly disappear, suggesting the amorphous structure of SOA-VO/Ipr (Fig. 2E). The HRTEM image displays very weak lattice fringes, confirming the enhanced amorphous degree of SOA-VO/Ipr in comparison to the VO/Et (Fig. 2C). As for Ibu molecules coupling, the FDA-VO/Ibu shows the same XRD pattern as SOA-VO/Ipr, but the HRTEM image does not show any lattice fringe, revealing a full degree of amorphization (Fig. 2, D and E). These results reveal that the amorphous degree of V_2O_5 is positively correlated with the chain length of the coupled alcohol molecules. Specifically, short-chain length Et leads to slight lattice distortions and weakens the crystallinity of V_2O_5, while moderate chain length Ipr induces a quasi-amorphous structure of V_2O_5, and longer chain length Ibu completely disrupts the crystal structure and results in the formation of a full amorphous structure.

Chemical environment and structural analysis of V_2O_5 modified with AMC

The hydroxyl oxygen atom, with two lone pairs of electrons, readily forms coordination bonds with electron-deficient centers of metal (*26*, *29*–*31*). In V_2O_5, V, as a five-electron–deficient acceptor, strongly interacts with the lone pairs on O atoms, inducing notable changes in its chemical environment upon bonding. Therefore, to confirm this bonding interaction, we performed Fourier transform infrared
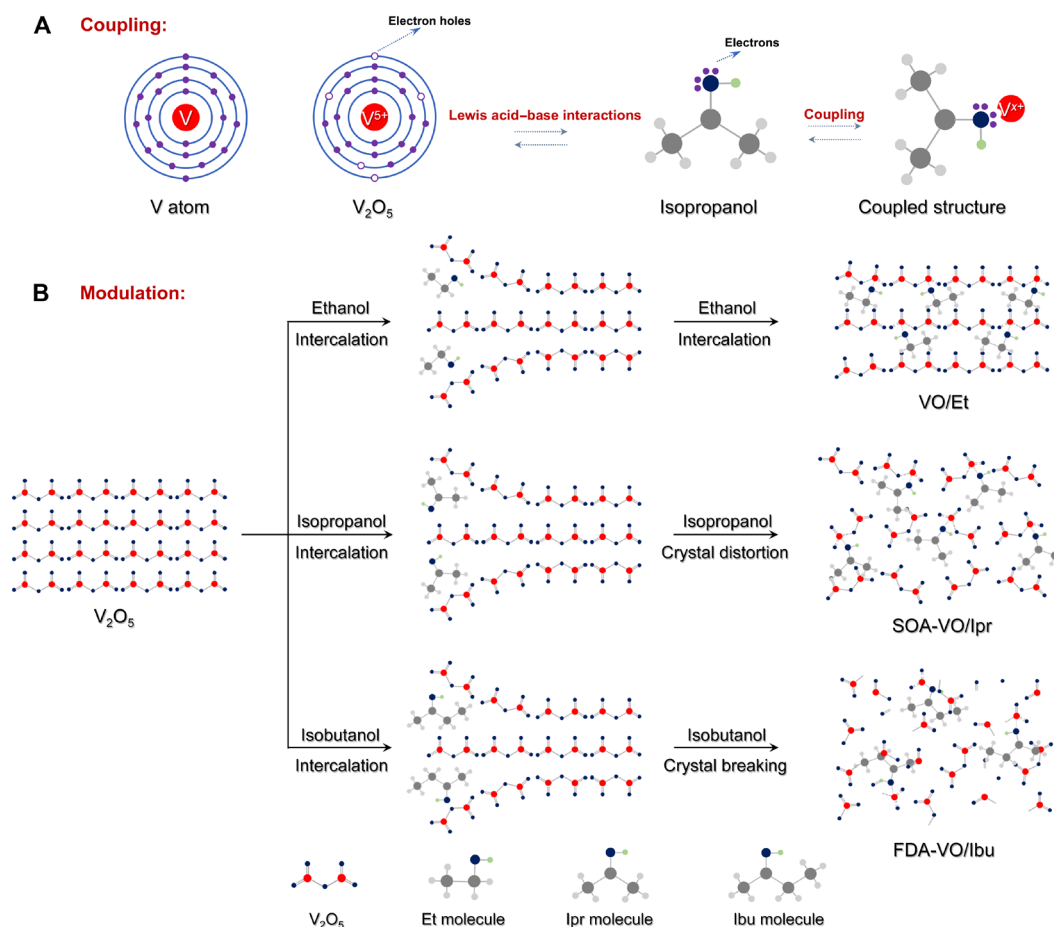
Fig. 1. Synthetic routine and mechanism schematic diagram. (**A**) Coupling mechanism of V_2O_5 with Et, Ipr, and Ibu. (**B**) The mechanism of alcohol molecules modulates V_2O_5.

spectroscopy (FTIR), Raman spectroscopy, x-ray photoelectron spectroscopy (XPS), ab initio molecular dynamics (AIMD) simulations, and DFT to systematically investigate the chemical environment of V after coupling. In FTIR spectrum, the peaks at 3414.8 and 1605 cm^{-1} correspond to the stretching and bending vibration modes of —OH, respectively, which are related to the presence of adsorbed water in the air and —OH in Et, Ipr, and Ibu (Fig. 2F) (*26, 32, 33*). The peaks at 2925.3, 1383.1, and 1129.2 cm^{-1} belong to the vibrations of —CH$_3$ and C—O bonds (*31, 32*), originating from the Et, Ipr, and Ibu molecules. In addition, the peaks at 985.1, 815.5, and 546.9 cm^{-1} are attributed to the V=O, V—O—V, and V—O bonds, respectively. Compared with pristine V_2O_5, the three bonds shift to lower wave numbers, indicating that the coupling effect weakens these bond strengths due to the structural distortion of the V_2O_5 lattice (*31, 34*). In addition, the V—O—V bonds are notably weakened because of the coupling between the electron-deficient V and the electron-donating O, which disrupts the ordered V—O—V arrangement (*26*). Furthermore, the Raman spectra of VO/Et, SOA-VO/Ipr, and FDA-VO/Ibu exhibit multiple V—O, V=O, and V—O—V vibrational modes similar to the pristine V_2O_5 crystal (fig. S6A). This indicates that some intact bonds still remain, although the Et, Ipr, and Ibu molecules disrupt the crystal structure of V_2O_5. However, two new peaks emerge at 840.2 and 876.4 cm^{-1} in the coupled

system, especially for SOA-VO/Ipr and FDA-VO/Ibu (fig. S6, B to E), corresponding to the vibrations of the C—O/C—C bonds and the —CH$_3$ group (*35–37*). This result confirms the successful coupling of the Et, Ipr, and Ibu molecules with V_2O_5. Notably, the splitting of the O—V—O vibration peak at 288.8 cm^{-1} is due to the coupling of —OH with V, which alters the symmetry of the crystal structure, causing peak splitting. Meanwhile, the V—OH interaction changes the charge distribution around V, resulting in a red shift of the vibration peaks at 290.6, 700, and 1000 cm^{-1} (*38*). The successful coupling of alcohol molecules with V_2O_5 was further confirmed by the energy-dispersive x-ray spectroscopy (EDS) elemental mapping (fig. S7), where the C signal originates from the alcohol molecules. The effective bonding between —OH groups and V is supported by AIMD. As shown in Fig. 2G and fig. S8, after 80 ps of simulation, the charge-imbalanced V tightly bonds with the electron-donating —OH, maintaining a stable structure. It demonstrates that the coupling between alcohol molecules and V_2O_5 can occur through V—OH coordinate bonds. Furthermore, the charge density difference and Bader charges are used to directly visualize the formation of V—OH bonds and charge transfer between V_2O_5 and alcohol molecules, as shown in fig. S9. The differential charge density reveals electron donation from O atoms in the —OH groups to V atoms, resulting in electron accumulation at V sites and depletion at —OH groups. Bader charge analysis quantifies
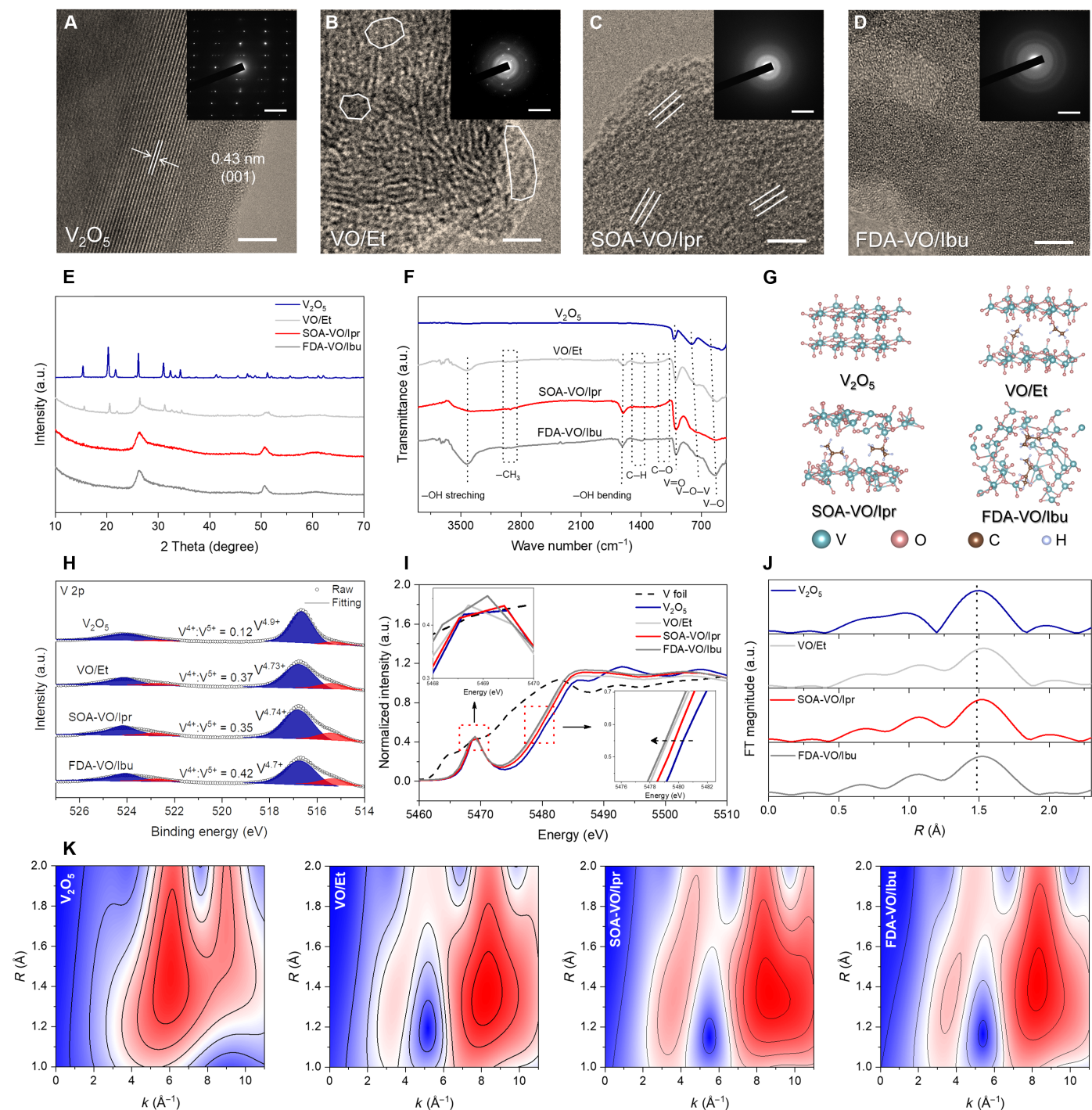
Fig. 2. Modulate mechanism, chemical environment, and structural analysis. (**A** to **D**) HRTEM images of V_2O_5, VO/Et, SOA-VO/Ipr, and FDA-VO/Ibu. Scale bars, 5 nm. Insets: Electron diffraction patterns. Scale bars, 5 nm^{-1}. (**E**) XRD pattern of V_2O_5, VO/Et, SOA-VO/Ipr, and FDA-VO/Ibu. (**F**) FTIR spectra of V_2O_5, VO/Et, SOA-VO/Ipr, and FDA-VO/Ibu. (**G**) AIMD molecular simulations of V_2O_5, VO/Et, SOA-VO/Ipr, and FDA-VO/Ibu. (**H**) V 2p XPS spectra of V_2O_5, VO/Et, SOA-VO/Ipr, and FDA-VO/Ibu. (**I**) XANES of V foil, V_2O_5, VO/Et, SOA-VO/Ipr, and FDA-VO/Ibu. (**J**) EXAFS spectra of V_2O_5, VO/Et, SOA-VO/Ipr, and FDA-VO/Ibu. (**K**) WTs of V K-edge EXAFS of V_2O_5, VO/Et, SOA-VO/Ipr, and FDA-VO/Ibu. a.u., arbitrary units.

this electron transfer, yielding ΔQ values of 0.51, 0.86, and 0.67 e for systems coupled with Et, Ipr, and Ibu molecules, confirming electron gain in all three systems upon coupling and providing evidence for V—OH bond formation. Therefore, they confirm that alcohol molecules coupled with V_2O_5 via V—OH bonding, wherein —OH donates lone-pair electrons and V serves as an electron acceptor to form robust interaction driven by Lewis acid–base interactions. The charge transfer between —OH and V atoms was further confirmed by XPS (Fig. 2H). The XPS analysis of V exhibited lower average valence for VO/Et (~+4.73), SOA-VO/Ipr (~+4.74), and FDA-VO/Ibu (~+4.7) compared to pristine V_2O_5 (~+4.9), indicating electron transfer from —OH to V through V—OH bond formation. The successful coupling of alcohol molecules is further supported by the XPS analysis of O 1s and C 1s, thermogravimetric analysis, and nuclear magnetic resonance (NMR), as shown in the additional results in figs. S10 to S13.

X-ray absorption spectroscopy techniques further confirm the coordination environment of V_2O_5 and its interaction with —OH groups. As presented in Fig. 2I, the chemical states of the VOs were investigated through V K-edge x-ray absorption near-edge structure (XANES) spectroscopy. The distinct pre-edge peak observed at approximately 5470 eV corresponds to the dipole-forbidden (1s → 3d) electronic transition, which becomes dipole-allowed because of hybridization between the metal 3d and ligand 2p orbitals as the local symmetry around V decreases (31, 39). Relative to metallic V foil, the pronounced pre-edge peak in V_2O_5 is attributed to the intrinsic asymmetry of its VO_5 coordination units (40). Notably, VO/Et, SOA-VO/Ipr, and FDA-VO/Ibu exhibit even more intense pre-edge features compared to pristine V_2O_5, underscoring the further disruption of symmetry in the VO_5 units induced by —OH group coordination. Furthermore, the leftward shift of the V K-edge positions for VO/Et, SOA-VO/Ipr, and FDA-VO/Ibu compared to pristine V_2O_5 indicates a reduction in the oxidation state of V. This shift results from the donation of lone-pair electrons by the —OH groups to the electron-deficient V centers, thereby filling the partially vacant electronic orbitals. We further conducted extended x-ray absorption fine structure (EXAFS) to study the coordination environment of alcohol molecule–coupled V_2O_5 (Fig. 2J, fig. S14, and table S1). As shown in the fitting curves in fig. S14, the typical peaks at 1.53 and 2.64 Å correspond to V—O and V—V (V—O—V) scattering paths, respectively. Compared to the V—O bond length in V_2O_5 ($R = 1.47$), the V—O bonds in the other three samples are slightly longer ($R = 1.54$ for SOA-VO/Ipr) because of the formation of coordinate bonds between V and —OH (Fig. 2J). On the basis of the fitting data from EXAFS results, the detailed V coordination numbers were presented in table S1, where the coordination number of V is approximately 3.1 in VO/Et, 3.4 in SOA-VO/Ipr, and 3.0 in FDA-VO/Ibu. Compared to crystalline V_2O_5 with a high coordination number of 5 for V, the lower coordination number of coupled V_2O_5 results from the destruction of the V_2O_5 crystal structure, which breaks the VO_5 units. This leads to an overall decrease in the average coordination number. Figure 2K shows the wavelet transformation (WT) of V K-edge EXAFS oscillations for the four samples. The k value corresponding to V—O increases because of the bonding between —OH and V, which changes the chemical environment around V—O.

Therefore, the aforementioned results demonstrate the coupling of V_2O_5 with alcohol molecules via Lewis acid–based interactions between V and —OH. This coupling induced a reduction in the valence state of V and a reconstruction of the crystalline structure in V_2O_5. In detail, alcohol molecules with varying chain lengths disrupt the crystalline structure of V_2O_5 to achieve different degrees of amorphization, with their —OH specifically used for coupling with V_2O_5. The coupling strength is determined by the electron-donating ability of —OH (41, 42), which is influenced by the electron-donating effects of attached methyl/ethyl groups (43, 44). Symmetric methyl groups exhibit stronger and more uniform electron donation, while asymmetric structures weaken this effect (45–47). Consequently, Ipr, with the strongest electron-donating —OH, achieves the highest coupling strength with V_2O_5. Theoretical calculations of V—OH bond energies (fig. S15) for VO/Et (43.27 kJ mol^{-1}), SOA-VO/Ipr (72.14 kJ mol^{-1}), and FDA-VO/Ibu (58.03 kJ mol^{-1}) confirm the superior coupling strength between Ipr and V_2O_5 due to its robust electron-donating capability. This enhanced coupling notably contributes to improved structural stability.

Analysis of V solubility and kinetics of V_2O_5

To establish the structure-performance relationship, we further evaluated the stability and Zn^{2+} storage kinetics of V_2O_5, VO/Et, SOA-VO/Ipr, and FDA-VO/Ibu. DFT studies (Fig. 3A) first confirmed that the pristine V_2O_5 shows a negative binding energy (−0.32 eV) toward H_2O, suggesting the good hydrophily of V_2O_5 that could facilitate the V_2O_5 hydrolysis and dissolution (48, 49) based on the spontaneous reaction of $V_2O_5 + 3H_2O = 2VO_2(OH)_2^- + 2H^+$ (fig. S16). In contrast, the binding energy of VO/Et slightly increases to −0.22 eV, leading to slight tolerance against V dissolution. Notably, the binding energy of FDA-VO/Ibu greatly enlarges to 0.38 eV, which was further improved to 1.00 eV after coupling V_2O_5 with Ipr molecules. This result indicates that SOA-VO/Ipr is difficult to bond with H_2O, thereby exhibiting the lowest solubility in aqueous solution. These theoretical analyses align closely with the dissolution experiments, where pristine V_2O_5 exhibits substantial V dissolution after 30 days of soaking in the electrolyte. In contrast, the dissolution of AMC-treated VOs is substantially suppressed (fig. S17). Compared to VO/Et and FDA-VO/Ibu, SOA-VO/Ipr exhibits better transparency in the electrolyte, confirming that the Ipr molecule has the best coupling ability to prevent V dissolution. In addition, a static electrochemical assessment of V dissolution was performed through open-circuit voltage (OCV) resting tests (17). Fully charged batteries were rested for 72 hours to analyze the relationship between recoverable capacity and structural stability, reflecting V solubility in the electrolyte. As illustrated in Fig. 3B, SOA-VO/Ipr exhibits charge and discharge capacity retention ratios (CCR and DCR) of 99.7 and 91.8% after resting, notably surpassing the ratios observed for V_2O_5 (90.4 and 83%), VO/Et (92.2 and 84.8%), and FDA-VO/Ibu (94 and 87.1%). This comparison demonstrates the high feasibility of SOA-VO/Ipr in suppressing V dissolution. Moreover, it was observed that SOA-VO/Ipr exhibits the highest cycling stability over 250 cycles at a low current density of 0.5 A g^{-1}, with a capacity decay rate of only 0.08% per cycle, which is substantially lower than those of V_2O_5 (0.43%), VO/Et (0.21%), and FDA-VO/Ibu (0.17%), as shown in Fig. 3C. It confirmed that Ipr molecules reinforce the stability of the SOA structure and thus effectively suppress V dissolution. This was further confirmed by the V dissolution content in the electrolyte after cycling, as determined by inductively coupled plasma (ICP) analysis (table S2). Notably, the SOA-VO/Ipr cathode exhibited the lowest dissolution content of 1.73 μg ml^{-1}. In addition, further data on the dissolution of V and evidence supporting the critical role of Ipr molecules are provided in figs. S18 to S23.
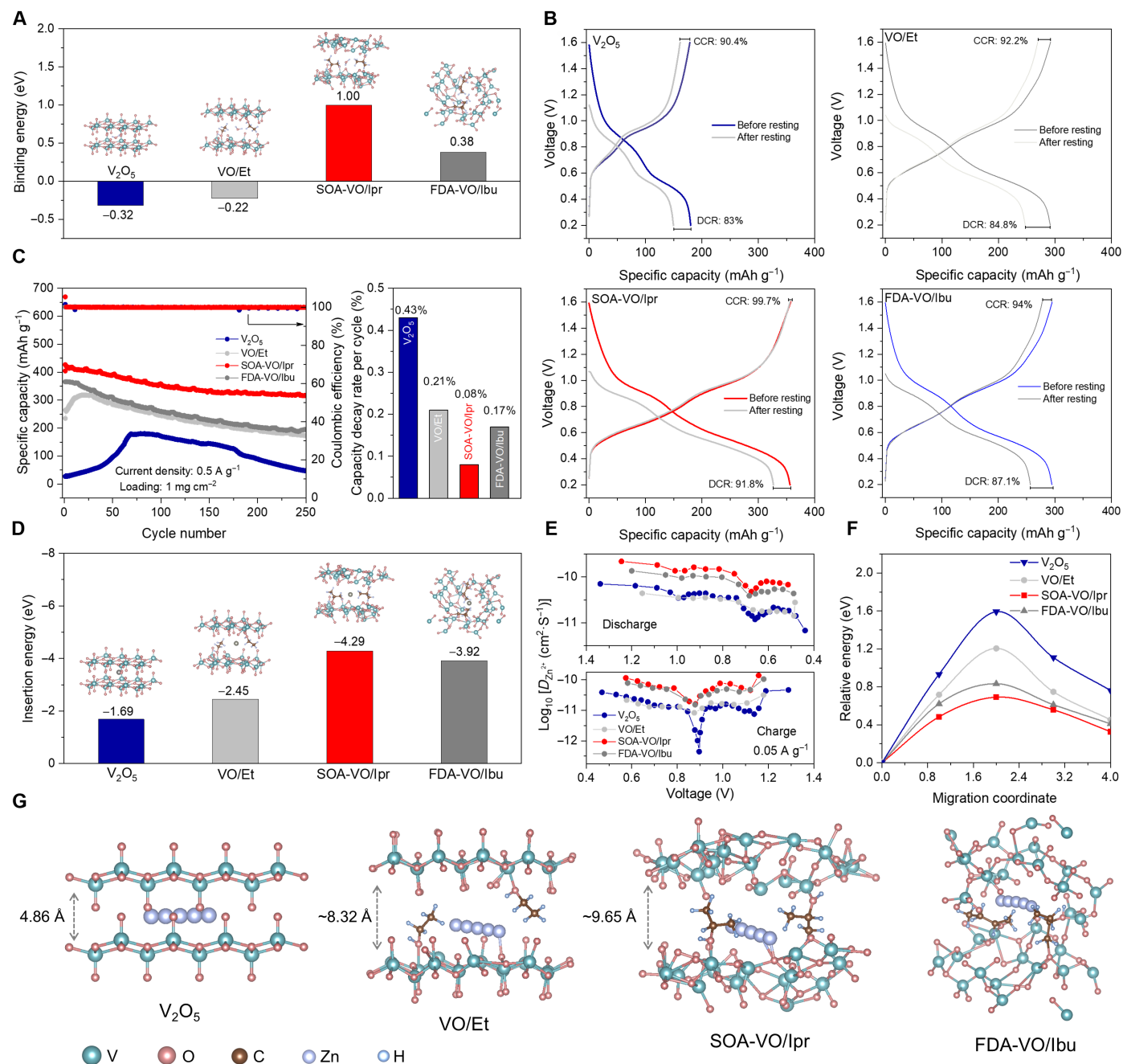
Fig. 3. Analysis of solubility and kinetics. (**A**) Binding energies of V_2O_5, VO/Et, SOA-VO/Ipr, and FDA-VO/Ibu with water molecules. (**B**) OCV resting experiments of V_2O_5, VO/Et, SOA-VO/Ipr, and FDA-VO/Ibu. (**C**) Cycling performance and capacity decay rate of V_2O_5, SOA-VO/Ipr, VO/Et, and FDA-VO/Ibu at 0.5 A g^{-1}. (**D**) Insertion energies of Zn^{2+} in V_2O_5, VO/Et, SOA-VO/Ipr, and FDA-VO/Ibu. (**E**) Ion diffusion coefficient of V_2O_5, VO/Et, SOA-VO/Ipr, and FDA-VO/Ibu. (**F**) Diffusion energy barriers of Zn^{2+} in the four materials. (**G**) Diffusion pathways of Zn^{2+} in the four materials.

On the other hand, to explore the relationship between structure and kinetics, we first perform DFT calculations to simulate the insertion energies of Zn^{2+} in V_2O_5, VO/Et, SOA-VO/Ipr, and FDA-VO/Ibu with optimized structures after Zn^{2+} insertion, as shown in Fig. 3D. The theoretical results indicated that SOA-VO/Ipr has the lowest Zn^{2+} insertion energy of −4.29 eV in comparison to V_2O_5 (−1.69 eV), VO/Et (−2.45 eV), and FDA-VO/Ibu (−3.92 eV), indicating fastest Zn^{2+} insertion/extraction kinetics in SOA-VO/Ipr. Furthermore, the

galvanostatic intermittent titration technique (GITT) analyses further highlighted the kinetic behavior and diffusion characteristics, as shown in Fig. 3E. On the basis of GITT, it was observed that SOA-VO/Ipr shows the highest Zn^{2+} diffusion coefficient, ranging from 4.78×10^{-11} to 2.19×10^{-10} cm^2 s^{-1} during discharging and 1.61×10^{-11} to 1.38×10^{-10} cm^2 s^{-1} during charging. However, note that FDA-VO/Ibu demonstrates a diffusion coefficient comparable to that of SOA-VO/Ipr, which can be attributed to the enhanced

reaction kinetics of its amorphous structure (9, 13). In addition, Fig. 3 (F and G) shows the Zn^{2+} diffusion energy barriers along the optimal Zn^{2+} diffusion pathways, wherein Zn^{2+} exhibits the lowest diffusion energy barrier (0.69 eV) and the most unimpeded diffusion pathways in SOA-VO/Ipr (~9.65 Å), indicating that SOA-VO/Ipr offers a facile transport channel for Zn^{2+}. Overall, we conclude that short-range ordered amorphous structure effectively shortens the Zn^{2+} diffusion path and broadens the transport channels, thereby enhancing the reaction kinetics.

Electrochemical performance and reaction mechanism of V_2O_5

The above analysis demonstrates that the close combination between V_2O_5 and Ipr molecules generates a highly stable structure that resists V dissolution, as well as an optimal amorphous structure that facilitates fast Zn^{2+} diffusion within the bulk structure. Consequently, SOA-VO/Ipr exhibits highly favorable reaction kinetics.

To further understand the charge storage mechanism, pseudocapacitive analysis was conducted on the basis of cyclic voltammetry (CV) curves at different scan rates (Fig. 4, A and B). The CV curves of SOA-VO/Ipr, recorded between 0.5 and 100 mV s^{-1}, reveal two pairs of reduction peaks (peak 3 and peak 4), corresponding to the conversion processes of V^{5+} to V^{4+} and V^{4+} to V^{3+}, respectively.

Peak 1 and peak 2 correspond to the oxidation process of V^{3+} to V^{5+}. In comparison to the CV curves of V_2O_5 at various scan rates (Fig. 4A), SOA-VO/Ipr exhibits a higher response current and larger peak area, indicating superior reaction kinetics and an increased Zn^{2+} storage capacity. To determine whether zinc-ion transfer is governed by capacitive control or diffusion control, we performed a linear fitting of the CV curves. The b values of SOA-VO/Ipr for peaks 1 to 4 were calculated to be 0.84, 0.92, 0.87, and 0.87, respectively (Fig. 4D). These values are close to 1 and higher than those of V_2O_5 (Fig. 4C), indicating a capacitive-controlled process, which explains the excellent reaction kinetics of SOA-VO/Ipr. The capacitance contribution is depicted in fig. S24, where an increase in scan rate leads to a higher capacitance contribution. At a scan rate of 10 mV s^{-1}, the capacitance contribution reaches 96.8%, indicating that SOA-VO/Ipr has extremely fast ion diffusion rates and outstanding rate performance. Figure 4E compares the rate performance of SOA-VO/Ipr and V_2O_5. SOA-VO/Ipr exhibits the best rate capability, achieving a remarkable discharge specific capacity of 219.4 mAh g^{-1} even at 100 A g^{-1}, substantially outperforming V_2O_5. When the current returns to 0.5 A g^{-1}, SOA-VO/Ipr maintains a specific capacity of 410 mAh g^{-1}, demonstrating a capacity retention ratio of 98.3% compared to the initial specific capacity of 417 mAh g^{-1}. Figure 4 (F and G) presents the charge-discharge curves at different rates for
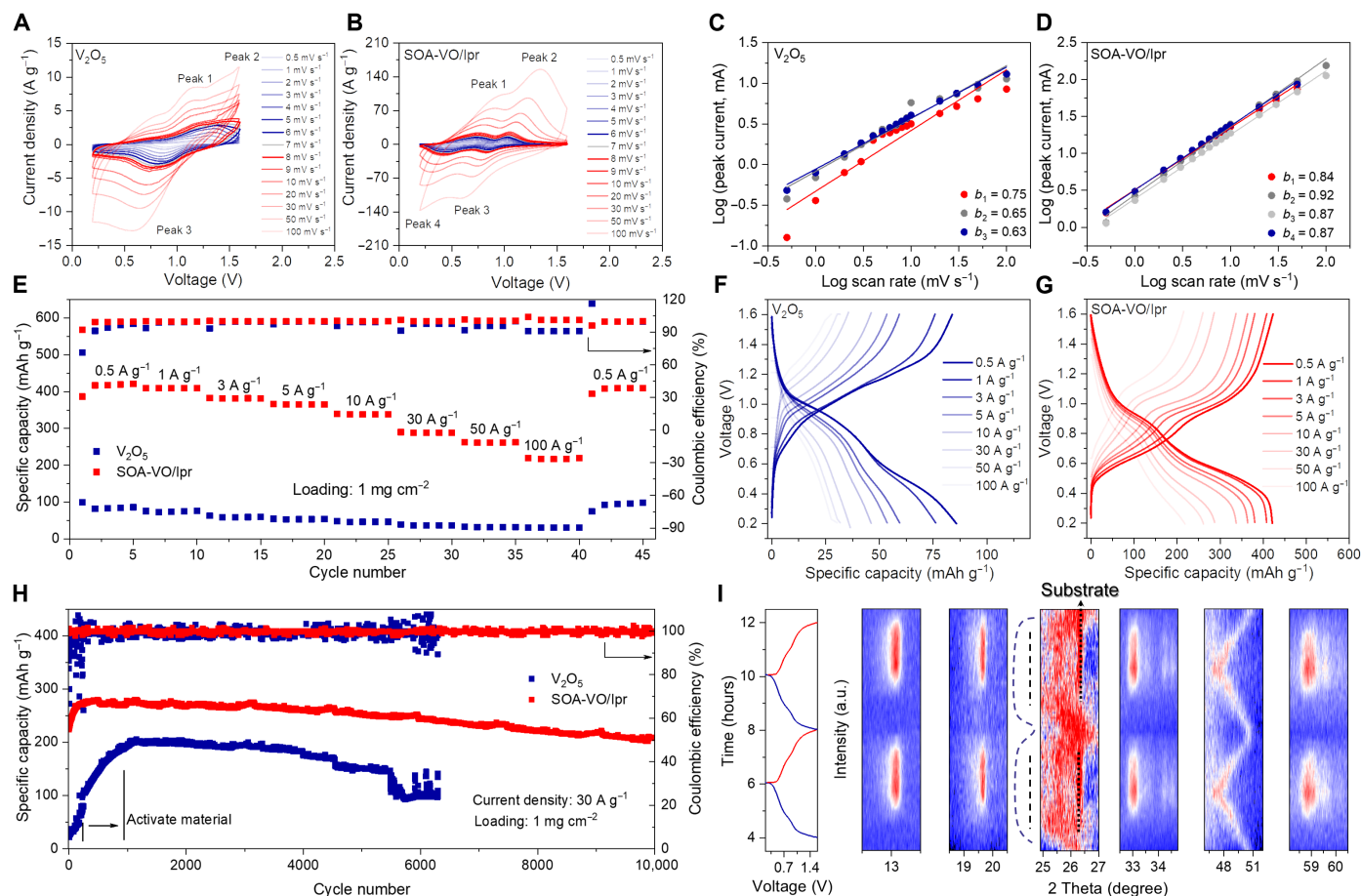

Fig. 4. The electrochemical performance and reaction mechanism. CV curves at different scan speeds of (**A**) V_2O_5 and (**B**) SOA-VO/Ipr. The fitted b value is based on the CV curves of (**C**) V_2O_5 and (**D**) SOA-VO/Ipr. (**E**) Rate performance of SOA-VO/Ipr and V_2O_5. Rate performance charge-discharge curves of (**F**) V_2O_5 and (**G**) SOA-VO/Ipr. (**H**) Long-term cycling performance at current density of 30 A g^{-1} of SOA-VO/Ipr and V_2O_5. (**I**) In situ XRD pattern of SOA-VO/Ipr.

V_2O_5 and SOA-VO/Ipr, respectively. Compared to V_2O_5, SOA-VO/Ipr exhibits a higher specific capacity at all current densities and displays well-defined charge-discharge plateaus even at a current density of 100 A g^{-1} (Fig. 4H), indicating faster Zn^{2+} transport within the SOA-VO/Ipr cathode. With a 200-fold current density increase (from 0.5 to 100 A g^{-1}), SOA-VO/Ipr retains 52.6% of its initial capacity. This outstanding rate performance surpasses that of most reported AZIB cathode materials (table S3), particularly considering that it is achieved without the addition of conductive carbon materials such as graphene or carbon nanotubes. In addition, SOA-VO/Ipr shows an exceptionally long cycling life, maintaining a high-capacity retention of 92.6% over 10,000 cycles at 30 A g^{-1} (Fig. 4H). After 10,000 cycles, SOA-VO/Ipr still retains an acceptable discharge capacity of 208 mAh g^{-1}, which is notably higher than that of V_2O_5. This indicates that SOA-VO/Ipr with durable short-range ordered amorphous structure provides efficient Zn^{2+} transport channels and abundant active sites (fig. S25), enabling excellent fast charge/discharge specific capacity. In contrast, V_2O_5 exhibits low specific capacity and sluggish reaction kinetics, necessitating an activation process exceeding 1000 cycles at 30 A g^{-1}. Kinetic performance is further evidenced by the electrochemical impedance spectroscopy (EIS) shown in fig. S26. After 30 cycles, SOA-VO/Ipr exhibits the lowest impedance value of 1.1 ohms, indicating that the amorphous structure and close coupling between SOA-VO and Ipr effectively enhance charge transfer kinetics, which accounts for the ultrahigh-rate performance of SOA-VO/Ipr. The more electrochemical results presented in figs. S27 to S30 further demonstrate that SOA-VO/Ipr exhibits the highest specific capacity and the fastest reaction kinetics.

We subsequently investigated the storage mechanism of the SOA-VO/Ipr cathode in AZIB using in situ XRD, ex situ XPS, and ex situ TEM tests. As shown in Fig. 4I and fig. S31, during discharge, the broad diffraction peaks (26.2° and 50.4°) shift to lower diffraction angles, indicating the zinc-ion intercalation into the SOA-VO/Ipr cathode. Meanwhile, distinct diffraction peaks at 13.1°, 19.6°, 33.1°, and 58.9° appear, corresponding to $Zn_x(CF_3SO_3)_y(OH)_{2x-y} \cdot nH_2O$ (50, 51). $Zn_x(CF_3SO_3)_y(OH)_{2x-y} \cdot nH_2O$ serves as the solid electrolyte interphase film on the cathode, which can continually self-optimize during cycling (50), ultimately enhancing the transport of zinc ions. The formation of $Zn_x(CF_3SO_3)_y(OH)_{2x-y} \cdot nH_2O$ also generates an equivalent number of protons (H^+), which tend to intercalate into the SOA-VO/Ipr electrode to maintain electrochemical neutrality during the discharge process (50). Therefore, the entire discharge process involves the co-intercalation of Zn^{2+} and H^+ (3, 50). During charging, the diffraction peaks of $Zn_x(CF_3SO_3)_y(OH)_{2x-y} \cdot nH_2O$ gradually disappear, and the amorphous characteristic peak returns to its initial position, demonstrating the highly reversible deintercalation process of Zn^{2+}/H^+. Throughout the entire discharge-charge process, the amorphous characteristic peaks exhibit the following lattice parameter changes:

26.2° → 25.65° → 26.2° (interlayer spacing, 3.41 Å → 3.46 Å → 3.41 Å) and

50.4° → 47.4° → 50.4° (interlayer spacing, 1.81 Å → 1.92 Å → 1.81 Å).

TEM analysis supports this dynamic process, showing that the initial lattice spacings of SOA-VO/Ipr at 0.34 and 0.181 nm, corresponding to the 26.2° and 50.4° peaks of the XRD pattern, expand to 0.347 and 0.191 nm during discharge and return to 0.341 and 0.181 nm upon recharging to 1.6 V (fig. S32). In comparison, pristine V_2O_5 also undergoes co-intercalation of Zn^{2+} and H^+, forming $H_xZn_{y-x}V_2O_5$ during the discharge process (51–53). However, because of its crystalline structure, pristine V_2O_5 exhibits substantially larger lattice spacing expansions, as shown in fig. S33. During discharge, the peak at 21° shifts to 19.27°, the peak at 26° shifts to 24.5°, and the peak at 30.65° shifts to 29.5°, corresponding to interlayer spacing expansions of 0.38, 0.21, and 0.11 Å, respectively. These expansions are notably greater than those observed for SOA-VO/Ipr, highlighting the superior buffering effect of the amorphous structure in mitigating lattice expansion. To further investigate the reaction mechanism of SOA-VO/Ipr, we performed ex situ XPS analysis (fig. S34). Using the sample after the first discharge-charge cycle as the initial state, the V 2p XPS spectrum can be deconvoluted into two peaks, corresponding to V^{5+} and V^{4+} (fig. S34A). During the discharge process, the proportion of the V^{5+} peak gradually decreases, while the V^{4+} peak increases. At a discharge potential of 0.2 V, the V^{5+} peak disappears completely, and a new V^{3+} peak emerges. Conversely, during the charging process, the V^{3+} peak gradually vanishes, accompanied by the reappearance and increase in the proportion of the V^{5+} peak. This demonstrates that the valence state of V undergoes dynamic changes during discharge and charge, consistent with the earlier electrochemical analysis. Throughout the process, the O 1s peak initially shifts toward higher binding energy and subsequently returns to its original position (fig. S34B). This phenomenon can be attributed to electron acquisition and subsequent electron loss by the V atom, leading to a redistribution of the O atomic electron cloud. The Zn 2p XPS demonstrates an initial increase in peak intensity, followed by a subsequent decline during both discharge and charge cycle, reflecting the intercalation and deintercalation mechanism of Zn^{2+} ions (fig. S34C). Therefore, the above results confirm the co-intercalation mechanism of Zn^{2+}/H^+, which is further validated by ex situ scanning electron microscopy (SEM), TEM, and EDS analyses, as shown in figs. S35 and S36.

We further observed that the SOA-VO/Ipr cathode has durable structural and chemical stability within repeated discharge/charge processes, as confirmed by various characterization techniques. As shown in fig. S37, the SOA-VO/Ipr cathode after the 50th discharge shows the representative amorphous diffraction peaks at 26.2° and 50.4° and the diffraction peaks of $Zn_x(CF_3SO_3)_y(OH)_{2x-y} \cdot nH_2O$, which disappear during the 50th charge and return to the amorphous peaks, confirming the reversible discharge/charge process. TEM analysis reveals that SOA-VO/Ipr retains its short-range ordered amorphous structure in both charged and discharged states after 50 cycles, which is further reflected in the broad diffraction rings observed in the SAED pattern (fig. S38). Furthermore, the XPS analysis of V 2p reveals the valence transition of SOA-VO/Ipr from +5/+4 in the charged state to +4/+3 in the discharged state (fig. S39A). Upon full discharge, a V^{3+} signal emerges, accounting for approximately 45%. After full charge, the V^{3+} signal disappears, and the proportion of V^{5+} increases to 61.7%. This observation clearly illustrates the dynamic valence changes of V during the charge-discharge process. The Zn 2p XPS results align with the previous analysis, confirming the intercalation and deintercalation of Zn^{2+} during the discharge/charge processes (fig. S39B). This conclusion is further supported by the EDS analysis (fig. S40). The atomic Zn/V ratio is around 1.66:1 after discharging to 0.2 V and 0.23:1 after a full charge to 1.6 V, demonstrating the reversible Zn^{2+}/H^+ intercalation and deintercalation in SOA-VO/Ipr. In addition, postcycling V K-edge XANES spectra of SOA-VO/Ipr demonstrate valence state variations of V during charge and discharge processes (fig. S41). The

edge shifts to lower energy in the discharge state and reverts to its original position upon charging, corroborating the reversible redox mechanism of V. Therefore, the above results confirm the co-intercalation mechanism of Zn^{2+}/H^+ and the structural stability of SOA-VO/Ipr, which provides a long cycle life for zinc-ion batteries.

Universal and practical application of AMC method

To explore the broad applicability of the AMC method, we extended our investigation beyond V_2O_5, such as VO_2, V_2O_3, and V_6O_{13}. As shown in the XRD patterns (fig. S42), all three VOs are initially in crystalline states, corresponding to monoclinic VO_2 ($P2_1/c$, PDF# 03-065-7960), hexagonal V_2O_3 (R3c, PDF#01-076-1043), and monoclinic V_6O_{13} (C2/m, PDF#01-089-0100). After coupling with alcohol molecules (Et, Ipr, or Ibu), XRD diffraction peaks are still

observed for V_2O_3, attributed to the poor oxidation ability of V^{3+}, which resists alcohol-induced reduction. In contrast, for VO_2 and V_6O_{13}, the XRD peaks gradually weaken, leaving only two broad peaks at 26.2° and 50.4° after coupling with Ipr and Ibu. This phase transition from crystalline to amorphous states follows a pattern similar to that of V_2O_5. The HRTEM images and corresponding SAED patterns further corroborate these findings. As shown in fig. S43, HRTEM and SAED images of V_2O_3 coupled with various alcohol-based organic molecules reveal no notable structural changes. However, for VO_2 and V_6O_{13}, sequential coupling with Et, Ipr, and Ibu molecules leads to progressive crystal lattice distortion (Fig. 5, B to I). Similar to V_2O_5, coupling with Et preserves the crystalline structure (Fig. 5, C and G), whereas coupling with Ipr and Ibu induces amorphous structures in VO_2 and V_6O_{13}. Specifically,
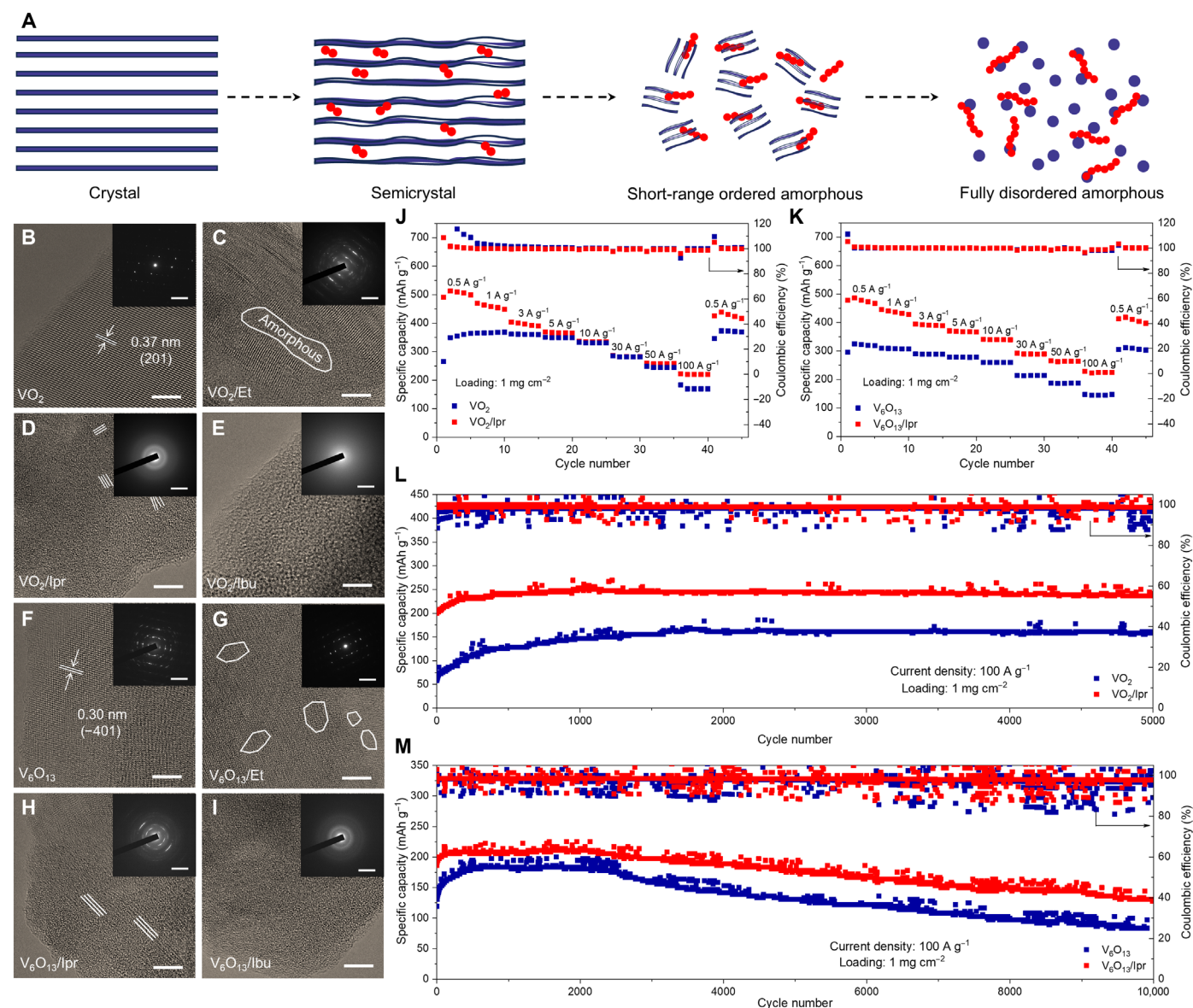

Fig. 5. Application of the universal AMC method. (**A**) Schematic diagram of crystal coupling alcohol-based molecules. (**B** to **I**) TEM images of VO_2, VO_2/Et, VO_2/Ipr, VO_2/Ibu, V_6O_{13}, V_6O_{13}/Et, V_6O_{13}/Ipr, and V_6O_{13}/Ibu. Scale bars, 5 nm. Insets: Electron diffraction patterns. Scale bars, 5 nm^{-1}. (**J**) Rate performance of VO_2 and VO_2/Ipr. (**K**) Rate performance of V_6O_{13} and V_6O_{13}/Ipr. (**L**) Long cycling performance of VO_2 and VO_2/Ipr. (**M**) Long cycling performance of V_6O_{13} and V_6O_{13}/Ipr.

VO$_2$/Ipr and V$_6$O$_{13}$/Ipr exhibit short-range ordered amorphous structures (Fig. 5, D and H), while VO$_2$/Ibu and V$_6$O$_{13}$/Ibu transition into fully disordered amorphous states (Fig. 5, E and I). The SAED patterns in the insets further validate this gradual transition. These results demonstrate that AMC is a universal method for modulating the amorphousness of VOs. The electrochemical performance of VO$_2$ (theoretical specific capacities, ~323.1 mAh g^{-1}) and V$_6$O$_{13}$ (theoretical specific capacities, ~417.4 mAh g^{-1}) (54, 55) was subsequently evaluated (Fig. 5, J to M). The rate performance of VO$_2$ and V$_6$O$_{13}$ before and after Ipr coupling is shown in Fig. 5 (J and K). Both VO$_2$/Ipr and V$_6$O$_{13}$/Ipr exhibit superior rate performance compared to their pristine counterparts, delivering specific capacities exceeding 200 mAh g^{-1} at an ultrahigh current density of 100 A g^{-1}. It confirms that short-range ordered amorphous structure is also well suited for enabling rapid and efficient Zn^{2+} transport pathways in VO$_2$/Ipr and V$_6$O$_{13}$/Ipr. The GITT results in fig. S44 reveal higher Zn^{2+} diffusion coefficients in VO$_2$/Ipr and V$_6$O$_{13}$/Ipr compared to their crystalline counterparts, VO$_2$ and V$_6$O$_{13}$, further validating the kinetic enhancement conferred by the unique structure facilitated by

Ipr molecules. In addition, long-term cycling tests (Fig. 5, L and M) demonstrate the remarkable stability of VO$_2$/Ipr and V$_6$O$_{13}$/Ipr, achieving durable cycling performances of 5000 and 10,000 cycles, respectively, at an ultrahigh current density of 100 A g^{-1}, notably outperforming their crystalline counterparts.

To address practical application requirements, we further assessed the performance of the AMC method under high-loading conditions and low electrolyte–to–active material (E/A) ratio (56). First, the SOA-VO/Ipr cathode in AZIB at a high-loading cathode of 20 mg cm^{-2} and a low E/A ratio of 7.5 μl mg^{-1} performed the durable repeated discharge/charge of 100 cycles at a low current density of 0.2 A g^{-1}, showing consistently high discharge specific capacities of above 350 mAh g^{-1}, with 91.2% retention after cycling and Coulombic efficiency of nearly 100% (Fig. 6A). It confirmed that the Ipr-coupled strategy enables the cathode with the high resistance to dissolution and thus realizes the stable cycling even at the challenging low current density (57, 58); in sharp contrast, sluggish reaction kinetics of V$_2$O$_5$ become more pronounced under high-loading conditions, thus requiring an extended activation period of
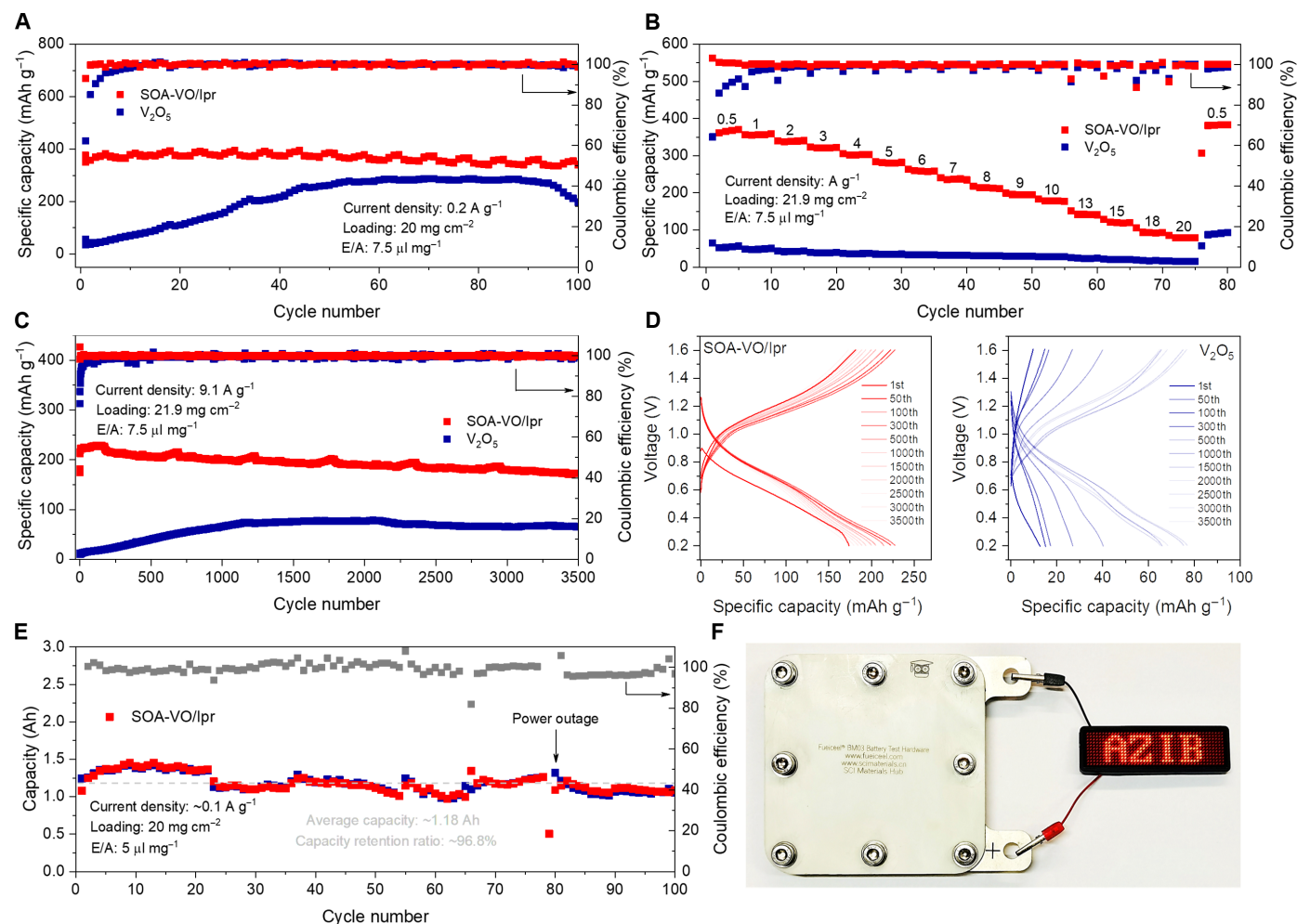

Fig. 6. The electrochemical performance under high loading. (**A**) Cycling performance of SOA-VO/Ipr and V$_2$O$_5$ at a current density of 0.2 A g^{-1}. The slight capacity fluctuation is attributed to room temperature variation caused by air conditioning system. (**B**) Rate performance comparison of SOA-VO/Ipr and V$_2$O$_5$. (**C**) Long-term cycling performance of SOA-VO/Ipr and V$_2$O$_5$ at a current density of 9.1 A g^{-1}. (**D**) Charge-discharge curves during long-term cycling of SOA-VO/Ipr and V$_2$O$_5$. (**E**) Cycling performance of the scale-up Zn//SOA-VO/Ipr battery. (**F**) Optical image of the scale-up battery powering an LED panel.

approximately 55 cycles. Even worse, its maximum discharge specific capacity is limited to 280 mAh g^{-1} at 90 cycles, beyond which the specific capacity rapidly declines because of consistent V dissolution and progressive structural collapse of V$_2$O$_5$ in aqueous electrolyte (Fig. 6A). The rate performance of high-loading cathodes further highlights the outstanding kinetics and reversibility of SOA-VO/Ipr compared to the V$_2$O$_5$ conditions, as shown in Fig. 6B. It was confirmed that the SOA-VO/Ipr cathode with a high loading of 21.9 mg cm^{-2} still delivers an acceptable discharge specific capacity of 183.1 mAh g^{-1} at a high current density of 10 A g^{-1} (areal current density, 219.1 mA cm^{-2}). It still exhibits a high discharge specific capacity of 381.1 mAh g^{-1} when returning to a low current density of 0.5 A g^{-1}. This remarkable rate performance is clearly beyond the capability of crystalline V$_2$O$_5$ (Fig. 6B). This difference, rooted in structural variations, becomes especially prominent for long-term cycling at high current densities (Fig. 6C). It was observed that the high-loading SOA-VO/Ipr of 21.9 mg cm^{-2} in AZIB demonstrated outstanding high-power performance at a high current density of 9.1 A g^{-1} (areal current density, 199.2 mA cm^{-2}), achieving stable cycling over 3500 cycles with a high discharge specific capacity of 228.8 mAh g^{-1} at 150 cycles and a minimal capacity decay rate of 0.0057% per cycle. This stands in stark contrast to the low discharge specific capacity of approximately 70 mAh g^{-1} observed in the high-loading V$_2$O$_5$ cathode under the high current density. Therefore, through a series of direct comparisons of high-loading performance, we confirm that the Ipr-coupled strategy effectively mitigates common issues of V dissolution in VOs. Moreover, the resulting short-range ordered amorphous structure fulfills the high-power requirements for practical battery applications. Accordingly, an ampere-hour–level scaled-up Zn//SOA-VO/Ipr battery with an electrode area of 7 × 7 cm^2, an SOA-VO/Ipr cathode of 20 mg cm^{-2}, and an E/A ratio of 5 µl mg^{-1} was assembled (Fig. 6E and fig. S45). It delivered reversible average discharge specific capacities of 1.18 Ah and powered the light-emitting diode (LED) light (Fig. 6F), showcasing its potential for practical energy storage applications.

DISCUSSION

In this work, we introduce a universal AMC method to regulate the amorphous degree and defect concentration in VO cathodes, thereby enhancing their performance. The process begins with alcohol molecules breaking the V—O bonds through their reducibility, subsequently by strong polar —OH—V interactions that induce coupling. Simultaneously, the degree of amorphousness is modulated by altering the chain length of the alcohol molecules. The use of alcohol molecules with varying chain lengths (Et, Ipr, and Ibu) allows for tailored modifications of the crystal structure, enabling precise control over the amorphousness of the VOs. In particular, the application of Ipr to V$_2$O$_5$ disrupts its layered crystalline structure, resulting in a moderate short-range ordered amorphous state (SOA-VO/Ipr). This coupling strategy effectively suppresses V dissolution and enhances reaction kinetics. As a result, the SOA-VO/Ipr cathode in AZIB achieves an impressive specific capacity of 219.4 mAh g^{-1} at super high 100 A g^{-1} and maintains an exceptional capacity retention of 92.6% over 10,000 cycles at 30 A g^{-1}. The assembled battery at a high-loading SOA-VO/Ipr cathode of 21.9 mg cm^{-2} for practical application still enables durable cycling for up to 3500 cycles at a high 9.1 A g^{-1} (199.2 mA cm^{-2}), with an impressive discharge capacity of 228.8 mAh g^{-1}. In addition, the universality of the AMC method was confirmed with VO$_2$ and V$_6$O$_{13}$, all of which demonstrated modulated amorphous characteristics and superior reaction kinetics, maintaining stable cycling for 10,000 cycles at 100 A g^{-1}. Therefore, we propose a groundbreaking and universal approach to regulate the amorphousness of V-based cathodes, enabling notable improvements in ion dynamics and effectively mitigating V dissolution. This strategy unlocks exciting opportunities for ultrafast battery technologies and paves the way for the development of advanced energy storage materials with superior capacity and performance.

MATERIALS AND METHODS
Materials
The following materials were used: V$_2$O$_5$ (99.6%; Sigma-Aldrich), Et (99.5%; Sigma-Aldrich), Ipr (99.5%; Sigma-Aldrich), Ibu (99.5%; Sigma-Aldrich), glucose (99.5%; Sigma-Aldrich), ammonium persulfate (98%; Sigma-Aldrich), oxalic acid (99%; Sigma-Aldrich), and zinc trifluoromethanesulfonate (98%; Sigma-Aldrich). Ketjenblack EC300J, zinc foil, titanium mesh, poly(tetrafluoroethylene), and sulfonated hydrophilic membrane were purchased from Canrd Technology Co. Ltd. The diameter of the zinc metal foil is 150 mm, and its thickness is 0.1 mm. The thickness of the titanium mesh is 0.1 mm (100 mesh).

Preparation of VO$_2$, V$_2$O$_3$, V$_2$O$_5$, and V$_6$O$_{13}$
For the preparation of VO$_2$, 100 mg of V$_2$O$_5$ and 100 mg of glucose were mixed with 20 ml of deionized water, sonicated for 20 min, and stirred for 30 min. The mixture was then transferred to a hydrothermal reactor and heated at 190°C for 15 hours. After heating, the product was washed three times with deionized water and dried at 80°C to obtain VO$_2$ (*59*).

For the preparation of V$_2$O$_3$, 500 mg of V$_2$O$_5$ was placed in a ceramic boat and reduced in a tube furnace under a hydrogen atmosphere at 700°C for 4 hours, with a heating rate of 5°C/min, to obtain V$_2$O$_3$.

For the preparation of V$_2$O$_5$, a specific amount of V$_2$O$_5$ powder (15.8 g) and ammonium persulfate (1.3 g) were dissolved in 720 ml of water and stirred at 55°C for 48 hours. The mixture was then washed three times with deionized water and Et, followed by freeze-drying for 24 hours. The resulting yellow powder was heated in a tube furnace at 350°C for 1 hour with a ramp rate of 5°C/min. After cooling, V$_2$O$_5$ plate samples were obtained (*60*).

For the preparation of V$_6$O$_{13}$, 1.2 g of V$_2$O$_5$ and 1.26 g of oxalic acid were mixed with 40 ml of deionized water, stirred for 120 min, and then transferred to a hydrothermal reactor. The mixture was heated at 180°C for 3 hours. After cooling to room temperature, the product was washed three times with deionized water and dried at 80°C to obtain V$_6$O$_{13}$ (*61*).

Preparation of VO/Et, SOA-VO/Ipr, SOA-VO, and FDA-VO/Ibu
For the preparation of SOA-VO/Ipr, 100 mg of the V$_2$O$_5$ plate was dissolved in 10 ml of Ipr, sonicated for 2 hours, and then sealed and heated at 80°C for 15 hours. After evaporating the solvent in a convection oven, SOA-VO/Ipr samples were obtained. VO/Et and FDA-VO/Ibu were prepared by replacing the Ipr with Et and Ibu, respectively, following the same procedure. SOA-VO was prepared by calcining the SOA-VO/Ipr sample at 280°C under an Ar atmosphere for 2 hours.

Characterization

Phase and structural analyses were conducted using an Empyrean XRD instrument. The sample morphology was observed with an SEM (S-3400N). High-resolution morphology was examined with a TEM (JEOL, JEM-F200, Japan), which was also equipped with EDS (X-Max80) for elemental composition and distribution analysis. Chemical state analysis was performed using an XPS spectrometer (Thermo Fisher Scientific, K-Alpha, USA). Raman spectroscopy to analyze chemical bond vibration modes was carried out using a HORIBA LabRAM HR Evolution instrument (Japan). Infrared analysis for organic functional groups was conducted using a Thermo Fisher Scientific Nicolet iS20 FTIR spectrometer (USA). The NMR ^{1}H spectra were measured using a Bruker Avance 400 instrument, with the samples dissolved in deuterated dimethyl sulfoxide. Content analysis was performed using a NETZSCH TG 209 F3 Tarsus thermogravimetric analyzer (Germany). V K-edge XANES was conducted at the Singapore Synchrotron Light Source. XAFS data were analyzed using ATHENA software (v.0.9.26) (62). WT-EXAFS analyses were performed using HAMA Fortran software (63). The Morlet function was selected as the mother wavelet, with parameters set to kappaMorlet = 3 and sigmaMorlet = 1, to enhance the resolution in k-space near the radial distance of interest ($R \approx 1.5$ Å). ICP spectroscopy (instrument: SHMADZU, ICPE-9820) was used to measure dissolved V content after 50 charge/discharge cycles. Separators were immersed in 2% dilute nitric acid for 24 hours, and the extracted solution was analyzed against standard solutions for accurate quantification of V dissolution.

Electrochemical characterization

For conventional electrode preparation, the cathode active material, conductive agent (Ketjenblack EC300J), and binder (PTFE) were mixed in a 7:2:1 mass ratio to form a homogeneous slurry. After grinding for 30 min, the mixture was rolled onto a titanium mesh cut into small discs with a diameter of 1.2 cm and dried. Each disc contained 1 to 1.2 mg of active material. For high active material loading electrodes, the cathode active material, conductive agent, and binder were mixed in a 7:2:0.5 mass ratio. The electrode diameters were 0.8 and 1.0 cm. The batteries were assembled using CR2025 coin cells, with zinc foil as the anode, glass fiber as the separator, and 2 M $Zn(CF_3SO_3)_2$ aqueous solution as the electrolyte. For scale-up assembly, 7×7 cm^2 electrodes with a loading of 20 mg cm^{-2} were used, and the electrolyte was added at 5 µl mg^{-1}. A composite separator composed of a sulfonated hydrophilic membrane and a glass fiber separator was applied to inhibit dendrite-induced cell shorting. Electrochemical performance tests, including EIS and CV, were conducted using a VMP3 multichannel potentiostat (BioLogic). GITT, cycling, and rate performance tests were performed using a Neware battery testing system.

GITT conditions involved 2 hours of rest, followed by 30 min of discharge/charge. Corresponding to the GITT curves, the diffusion coefficient of Zn^{2+} ions upon intercalation and extraction can be accurately evaluated by the following equation

$$D_{Zn^{2+}} = \frac{4}{\pi\tau}\left(\frac{m_B V_M}{M_B S}\right)^2 \left(\frac{\Delta E_S}{\Delta E_\tau}\right)^2 \quad (1)$$

where τ is the constant current pulse duration (in seconds), m_B is the mass loading, M_B is the molecular weight (in grams per mole), and V_M is the molar volume (in cubic centimeters per mole) of the active materials on the cathode. S corresponds to the contact area of the electrode-electrolyte interface. ΔE_τ is the total change of battery voltage during constant current pulse duration (τ) without considering voltage drop. ΔE_S corresponds to the change of steady-state voltage.

The calculation of the b value and the capacitive/diffusion-controlled process follows the equations below: The b value represents the slope of the logarithm of the peak current (i) versus the logarithm of the scan rate (v), reflecting whether the electrochemical process is diffusion controlled or capacitive controlled. A b value close to 1 indicates a capacitive-controlled process, while a b value of 0.5 indicates a diffusion-controlled process. The formula for calculating b is as follows

$$i = a * v^b \quad (2)$$

$$\log(i) = b * \log(v) + \log * (a) \quad (3)$$

The formula for calculating capacitive control and diffusion control is as follows

$$i = k_1 v + k_2 v^{\frac{1}{2}} \quad (4)$$

where $k_1 v$ is the capacitive control process and $k_2 v^{1/2}$ is the diffusion control process. EIS testing was performed over a frequency range of 0.01 Hz to 100 kHz. The CV testing window was set from 0.2 to 1.6 V.

Computational methods

We conducted all DFT calculations using the Vienna Ab initio Simulation Package (64, 65) within the framework of the generalized gradient approximation, as formulated by PBE (66) formulation. The ionic cores were represented using projected augmented wave potentials (67, 68), while the valence electrons were treated with a plane wave basis set using a kinetic energy cutoff of 450 eV. We used Gaussian smearing with a width of 0.05 eV to allow for partial occupancies of the Kohn-Sham orbitals. Self-consistency of the electronic energy was achieved when the energy variation was less than 10^{-5} eV. Geometry optimization was deemed convergent when the force change was below 0.05 eV Å^{-1}. To account for dispersion interactions, we applied Grimme et al.'s DFT-D3 correction (69). Structural optimizations were performed using gamma-point sampling for the k-points in the Brillouin zone. Adsorption energies (E_{ads}) were determined using the relation $E_{ads} = E_{ad/sub} - E_{ad} - E_{sub}$, where $E_{ad/sub}$, E_{ad}, and E_{sub} represent the total energies of the optimized adsorbate/substrate system, the isolated adsorbate, and the clean substrate, respectively. The transition states for elementary reaction steps were identified using the nudged elastic band method, wherein the reaction pathway between reactants and products was discretized into five intermediate images. These images were relaxed until the perpendicular forces were reduced to less than 0.05 eV Å^{-1}. The charge density difference of the system is as follows: $\Delta\rho = \rho total - \rho A - \rho B$, where $\rho total$ is the charge density of binding systems, while ρA and ρB are the subcharge densities.

Simulation methods

AIMD simulations were performed to investigate disordered structures. During the geometry optimization process, a cutoff energy of 450 eV was used. The Brillouin zone was sampled using a

Monkhorst-Pack k-point grid of $2 \times 2 \times 2$. To account for van der Waals interactions (*70*), the PBE-D3 dispersion correction was applied. The geometry optimization was carried out using the conjugate gradient method, with a smearing width of 0.1 eV. The convergence criteria for the total energy and forces were set at 10^{-5} eV per cell and 0.05 eV Å^{-1}, respectively. AIMD simulations were conducted over 80 ps for equilibration, with a time step of 1 fs, maintaining a constant temperature of 300 K in the Nosé-Hoover isokinetic ensemble.

Supplementary Materials
This PDF file includes:
Figs. S1 to S45
Tables S1 to S3
References

REFERENCE AND NOTES

1. D. Zhang, W. Wang, S. Li, X. Shen, H. Xu, Design strategies and energy storage mechanisms of MOF-based aqueous zinc ion battery cathode materials. *Energy Storage Mater.* **69**, 103436 (2024).
2. Z. Yi, G. Chen, F. Hou, L. Wang, J. Liang, Strategies for the stabilization of Zn metal anodes for Zn-ion batteries. *Adv. Energy Mater.* **11**, 2003065 (2021).
3. Y. Li, Z. Wang, Y. Cai, M. E. Pam, Y. Yang, D. Zhang, Y. Wang, S. Huang, Designing advanced aqueous zinc-ion batteries: Principles, strategies, and perspectives. *Energy Environ. Mater.* **5**, 823–851 (2022).
4. T. Xiong, Y. Zhang, W. S. V. Lee, J. Xue, Defect engineering in manganese-based oxides for aqueous rechargeable zinc-ion batteries: A review. *Adv. Energy Mater.* **10**, 2001769 (2020).
5. F. Wan, Z. Niu, Design strategies for vanadium-based aqueous zinc-ion batteries. *Angew. Chem. Int. Ed. Engl.* **131**, 16508–16517 (2019).
6. Z. Li, T. Liu, R. Meng, L. Gao, Y. Zou, P. Peng, Y. Shao, X. Liang, Insights into the structure stability of prussian blue for aqueous zinc ion batteries. *Energy Environ. Mater.* **4**, 111–116 (2021).
7. J. Cui, Z. Guo, J. Yi, X. Liu, K. Wu, P. Liang, Q. Li, Y. Liu, Y. Wang, Y. Xia, J. Zhang, Organic cathode materials for rechargeable zinc batteries: Mechanisms, challenges, and perspectives. *ChemSusChem* **13**, 2160–2185 (2020).
8. X. Chen, H. Zhang, J.-H. Liu, Y. Gao, X. Cao, C. Zhan, Y. Wang, S. Wang, S.-L. Chou, S.-X. Dou, Vanadium-based cathodes for aqueous zinc-ion batteries: Mechanism, design strategies and challenges. *Energy Storage Mater.* **50**, 21–46 (2022).
9. Z. Wang, Y. Song, J. Wang, Y. Lin, J. Meng, W. Cui, X.-X. Liu, Vanadium oxides with amorphous-crystalline heterointerface network for aqueous zinc-ion batteries. *Angew. Chem. Int. Ed. Engl.* **62**, e202216290 (2023).
10. Y. Li, D. Zhang, S. Huang, H. Y. Yang, Guest-species-incorporation in manganese/vanadium-based oxides: Towards high performance aqueous zinc-ion batteries. *Nano Energy* **85**, 105969 (2021).
11. T. Xiong, Z. G. Yu, H. Wu, Y. Du, Q. Xie, J. Chen, Y.-W. Zhang, S. J. Pennycook, W. S. V. Lee, J. Xue, Defect engineering of oxygen-deficient manganese oxide to achieve high-performing aqueous zinc ion battery. *Adv. Energy Mater.* **9**, 1803815 (2019).
12. Y. Li, X. Liu, M. Zhang, D. Sheng, P. Ren, L. Che, X. Wang, Z. X. Shen, Optimization strategy of surface and interface in electrolyte structure of aqueous zinc-ion battery. *ACS Mater. Lett.* **6**, 1938–1960 (2024).
13. S. Deng, Z. Yuan, Z. Tie, C. Wang, L. Song, Z. Niu, Electrochemically induced metal-organic-framework-derived amorphous V_2O_5 for superior rate aqueous zinc-ion batteries. *Angew. Chem. Int. Ed. Engl.* **59**, 22002–22006 (2020).
14. Q. Shi, S. M. Moinuddin, Y. Wang, F. Ahsan, F. Li, Physical stability and dissolution behaviors of amorphous pharmaceutical solids: Role of surface and interface effects. *Int. J. Pharm.* **625**, 122098 (2022).
15. P. A. Priemel, H. Grohganz, K. C. Gordon, T. Rades, C. J. Strachan, The impact of surface-and nano-crystallisation on the detected amorphous content and the dissolution behaviour of amorphous indomethacin. *Eur. J. Pharm. Biopharm.* **82**, 187–193 (2012).
16. G. G. Z. Zhang, D. Zhou, "Crystalline and amorphous solids" in *Developing Solid Oral Dosage Forms* (2017), pp. 23–57.
17. Z. Chen, H. Liu, S. Fan, Q. Zhang, C. Yuan, W. Peng, Y. Li, X. Fan, Inhibition of vanadium cathode dissolution in zinc-ion batteries on thermodynamics and kinetics by guest pre-intercalation. *Adv. Energy Mater.* **14**, 2400977 (2024).
18. D. Bin, W. Huo, Y. Yuan, J. Huang, Y. Liu, Y. Zhang, F. Dong, Y. Wang, Y. Xia, Organic-inorganic-induced polymer intercalation into layered composites for aqueous zinc-ion battery. *Chem* **6**, 968–984 (2020).
19. L. Zhang, J. Hu, B. Zhang, J. Liu, H. Wan, L. Miao, J. Jiang, Suppressing cathode dissolution via guest engineering for durable aqueous zinc-ion batteries. *J. Mater. Chem. A* **9**, 7631–7639 (2021).
20. D. Zhang, J. Cao, Y. Yue, T. Pakornchote, T. Bovornratanaraks, J. Han, X. Zhang, J. Qin, Y. Huang, Two birds with one stone: Boosting zinc-ion insertion/extraction kinetics and suppressing vanadium dissolution of V_2O_5 via La^{3+} incorporation enable advanced zinc-ion batteries. *ACS Appl. Mater. Interfaces* **13**, 38416–38424 (2021).
21. J. He, L. Fang, Controllable synthesis of reduced graphene oxide. *Curr. Appl. Phys.* **16**, 1152–1158 (2016).
22. T. Nakayama, N. Okumura, B. Uno, Complementary effect of intra-and intermolecular hydrogen bonds on electron transfer in β-hydroxy-anthraquinone derivatives. *J. Phys. Chem. B* **124**, 848–860 (2020).
23. C. R. Myers, K. H. Nealson, Bacterial manganese reduction and growth with manganese oxide as the sole electron acceptor. *Science* **240**, 1319–1321 (1988).
24. B. Li, Y. Tao, Z. Mao, Q. Gu, Y. Han, B. Hu, H. Wang, A. Lai, P. Xing, Q. L. Wu, Iron oxides act as an alternative electron acceptor for aerobic methanotrophs in anoxic lake sediments. *Water Res.* **234**, 119833 (2023).
25. X. Ren, Y. Liu, W. Guo, Morphology and crystal facet-dependent activation mechanism of persulfate by V_2O_5 nanomaterials for organic pollutants degradation. *Sep. Purif. Technol.* **253**, 117501 (2020).
26. X. Cheng, Z. Xiang, C. Yang, Y. Li, L. Wang, Q. Zhang, Polar organic molecules inserted in vanadium oxide with enhanced reaction kinetics for promoting aqueous zinc-ion storage. *Adv. Funct. Mater.* **34**, 2311412 (2023).
27. G. Luis, Isopropanol adsorption-oxidation over V_2O_5—A mass spectrometry study. *J. Mol. Catal. A Chem.* **247**, 31–35 (2006).
28. Y. Chhiti, N. Badri, F. Bentiss, M. Bensitel, "Propan-2-Ol (isopropanol) conversion to propene and acetone over V_2O_5 catalysts supported on activated carbon (AC)," in *Smart Application and Data Analysis for Smart Cities (SADASC'18)* (2018).
29. T. Wei, Z. Fan, G. Zhao, Enhanced adsorption and degradation of nonylphenol on electron-deficient centers of photocatalytic surfaces. *Chem. Eng. J.* **388**, 124168 (2020).
30. L. Lyu, L. Han, W. Cao, Y. Gao, Q. Zeng, G. Yu, X. Huang, C. Hu, Efficient Fenton-like process for organic pollutant degradation on Cu-doped mesoporous polyimide nanocomposites. *Environ. Sci. Nano* **6**, 798–808 (2019).
31. M. Liu, X. Li, M. Cui, F. Chen, J. Li, W. Shi, Y. Liu, X. Li, Y. Wang, W. Zhang, C. Shao, Y. Liu, Amorphous organic-hybrid vanadium oxide for near-barrier-free ultrafast-charging aqueous zinc-ion battery. *Nat. Commun.* **15**, 10769 (2024).
32. F. Rahmawati, F. R. Putri, A. Masykur, The photocatalytic activity of ZnS-TiO$_2$ on a carbon fiber prepared by chemical bath deposition. *Open Chem.* **17**, 132–141 (2019).
33. M. Del Arco, S. Gutierrez, C. Martin, V. Rives, FTIR study of isopropanol reactivity on calcined layered double hydroxides. *Phys. Chem. Chem. Phys.* **3**, 119–126 (2001).
34. C. Chen, J. Gao, Y. Yan, Observation of the type of hydrogen bonds in coal by FTIR. *Energy Fuels* **12**, 446–449 (1998).
35. K. Tanabe, Concentration dependence of Raman linewidth of isopropanol in aqueous solution. *J. Raman Spectrosc.* **15**, 248–251 (1984).
36. S. F. Rice, T. B. Hunter, R. G. Hanush, Raman spectroscopic measurement of oxidation in supercritical water. 2. Conversion of isopropyl alcohol to acetone. *Ind. Eng. Chem. Res.* **35**, 3984–3990 (1996).
37. B. Yang, X. Cao, S. Wang, C. Sun, Exploring molecular association of isopropanol-water binary solution by Raman spectroscopy. *Optik* **204**, 163544 (2020).
38. S. Dong, W. Shin, H. Jiang, X. Wu, Z. Li, J. Holoubek, W. F. Stickle, B. Key, C. Liu, J. Lu, P. A. Greaney, X. Zhang, X. Ji, Ultra-fast NH$_4^+$ storage: Strong H bonding between NH$_4^+$ and bi-layered V_2O_5. *Chem* **5**, 1537–1551 (2019).
39. J. Wong, F. W. Lytle, R. P. Messmer, D. H. Maylotte, K-edge absorption spectra of selected vanadium compounds. *Phys. Rev. B* **30**, 5596–5610 (1984).
40. G. P. Singh, P. Kaur, P. Kaur, D. P. Singh, Role of V_2O_5 in structural properties of V_2O_5-MnO$_2$-PbO-B$_2O_3$ glasses. *Mater. Phys. Mech.* **12**, 58–63 (2011).
41. Y. Kim, J. Hong, J. H. Oh, C. Yang, Naphthalene diimide incorporated thiophene-free copolymers with acene and heteroacene units: Comparison of geometric features and electron-donating strength of co-units. *Chem. Mater.* **25**, 3251–3259 (2013).
42. T. Sutradhar, A. Misra, Role of electron-donating and electron-withdrawing groups in tuning the optoelectronic properties of difluoroboron-napthyridine analogues. *J. Phys. Chem. A* **122**, 4111–4120 (2018).
43. X. An, H. Liu, Q. Li, B. Gong, J. Cheng, Influence of substitution, hybridization, and solvent on the properties of C-HO single-electron hydrogen bond in CH$_3$-H$_2O$ complex. *J. Phys. Chem. A* **112**, 5258–5263 (2008).
44. X. An, Q. Li, Strong effect of methyl group on the strength of ionic hydrogen bond between C$_2H_2$ and H$_3O^+$. *Int. J. Quantum Chem.* **109**, 870–875 (2009).
45. W. D. Tuttle, A. M. Gardner, L. E. Whalley, D. J. Kemp, T. G. Wright, Effects of symmetry, methyl groups and serendipity on intramolecular vibrational energy dispersal. *Phys. Chem. Chem. Phys.* **21**, 14133–14152 (2019).

46. J. Ge, L. Hong, H. Ma, Q. Ye, Y. Chen, L. Xie, W. Song, D. Li, Z. Chen, K. Yu, J. Zhang, Z. Wei, F. Huang, Z. Ge, Asymmetric substitution of end-groups triggers 16.34% efficiency for all-small-molecule organic solar cells. *Adv. Mater.* **34**, e2202752 (2022).

47. L. Siebe, C. Butenuth, A. Köhler, A. Stammler, J. Oldengott, H. Bögge, T. Glaser, Synthesis of asymmetricvariants in a dinucleating ligand family and application for dinuclear copper(II) complexes. *Eur. J. Inorg. Chem.* **27**, e202400142 (2024).

48. Y. Li, H. Ba, Z. Wang, S. Wu, Y. Shang, S. Huang, H. Y. Yang, Electrolyte pH and operating potential: Critical factors regulating the anodic oxidation and zinc storage mechanisms in aqueous zinc ion battery. *Mater. Today Energy* **39**, 101460 (2024).

49. Y. Lu, T. Zhu, W. van den Bergh, M. Stefik, K. Huang, A high performing Zn-ion battery cathode enabled by in situ transformation of V_2O_5 atomic layers. *Angew. Chem. Int. Ed. Engl.* **59**, 17004–17011 (2020).

50. W. Liang, D. Rao, T. Chen, R. Tang, J. Li, H. Jin, $Zn_{0.52}V_2O_{5-a}$·1.8H_2O cathode stabilized by in situ phase transformation for aqueous zinc-ion batteries with ultra-long cyclability. *Angew. Chem. Int. Ed. Engl.* **61**, e202207779 (2022).

51. W. Zhang, C. Zuo, C. Tang, W. Tang, B. Lan, X. Fu, S. Dong, P. Luo, The current developments and perspectives of V_2O_5 as cathode for rechargeable aqueous zinc-ion batteries. *Energ. Technol.* **9**, 2000789 (2020).

52. S. Linghu, J. Ye, K. Deng, P. Liu, Y. Zhong, T. You, W. Tian, J. Ji, Coupling of V_2O_5 structural design and electrolyte modulation toward stable zinc-ion battery. *J. Power Sources* **592**, 233922 (2024).

53. A. Guo, Z. Wang, L. Chen, W. Liu, K. Zhang, L. Cao, B. Liang, D. Luo, A comprehensive review of the mechanism and modification strategies of V_2O_5 cathodes for aqueous zinc-ion batteries. *ACS Nano* **18**, 27261–27286 (2024).

54. W. Deng, C. Li, W. Zou, X. Yu, Y. Chen, R. Li, Understanding the super-theoretical capacity behavior of VO_2 in aqueous Zn batteries. *Small* **20**, e2309527 (2024).

55. L. Chen, W. Zhang, J. Zhang, Q. An, Zn^{2+}-storage mechanism in V_6O_{13} with nanosheets for high-capacity and long-life aqueous zinc-metal batteries. *Chem. Commun.* **60**, 5968–5971 (2024).

56. G. Zampardi, F. La Mantia, Open challenges and good experimental practices in the research field of aqueous Zn-ion batteries. *Nat. Commun.* **13**, 687 (2022).

57. W. Zhang, S. Liang, G. Fang, Y. Yang, J. Zhou, Ultra-high mass-loading cathode for aqueous zinc-ion battery based on graphene-wrapped aluminum vanadate nanobelts. *Nanomicro Lett.* **11**, 69 (2019).

58. M. Wu, C. Shi, J. Yang, Y. Zong, Y. Chen, Z. Ren, Y. Zhao, Z. Li, W. Zhang, L. Wang, X. Huang, W. Wen, X. Li, X. Ning, X. Ren, D. Zhu, The LiV_3O_8 superlattice cathode with optimized zinc ion insertion chemistry for high mass-loading aqueous zinc-Ion batteries. *Adv. Mater.* **36**, e2310434 (2024).

59. Q. He, T. Hu, Q. Wu, C. Wang, X. Han, Z. Chen, Y. Zhu, J. Chen, Y. Zhang, L. Shi, X. Wang, Y. Ma, J. Zhao, Tunnel-oriented VO_2 (B) cathode for high-rate aqueous zinc-ion batteries. *Adv. Mater.* **36**, e2400888 (2024).

60. H. Liu, L. Jiang, B. Cao, H. Du, H. Lu, Y. Ma, H. Wang, H. Guo, Q. Huang, B. Xu, S. Guo, Van der Waals interaction-driven self-assembly of V_2O_5 nanoplates and MXene for high-performing zinc-ion batteries by suppressing vanadium dissolution. *ACS Nano* **16**, 14539–14548 (2022).

61. W. Shi, B. Yin, Y. Yang, M. B. Sullivan, J. Wang, Y.-W. Zhang, Z. G. Yu, W. S. V. Lee, J. Xue, Unravelling V_6O_{13} diffusion pathways via CO_2 modification for high-performance zinc ion battery cathode. *ACS Nano* **15**, 1273–1281 (2021).

62. B. Ravel, M. Newville, *ATHENA, ARTEMIS, HEPHAESTUS*: Data analysis for X-ray absorption spectroscopy using *IFEFFIT*. *J. Synchrotron Radiat.* **12**, 537–541 (2005).

63. H. Funke, A. C. Scheinost, M. Chukalina, Wavelet analysis of extended x-ray absorption fine structure data. *Phys. Rev. B* **71**, 094110 (2005).

64. G. Kresse, J. Furthmüller, Efficiency of ab-initio total energy calculations for metals and semiconductors using a plane-wave basis set. *Comput. Mater. Sci.* **6**, 15–50 (1996).

65. G. Kresse, J. Furthmüller, Efficient iterative schemes for ab initio total-energy calculations using a plane-wave basis set. *Phys. Rev. B Condens. Matter* **54**, 11169–11186 (1996).

66. J. P. Perdew, K. Burke, M. Ernzerhof, Generalized gradient approximation made simple. *Phys. Rev. Lett.* **77**, 3865–3868 (1996).

67. G. Kresse, D. Joubert, From ultrasoft pseudopotentials to the projector augmented-wave method. *Phys. Rev. B* **59**, 1758–1775 (1999).

68. P. E. Blöchl, Projector augmented-wave method. *Phys. Rev. B* **50**, 17953–17979 (1994).

69. S. Grimme, J. Antony, S. Ehrlich, H. Krieg, A consistent and accurate ab initio parametrization of density functional dispersion correction (DFT-D) for the 94 elements H-Pu. *J. Chem. Phys.* **132**, 154104 (2010).

70. G. Henkelman, B. P. Uberuaga, H. Jónsson, A climbing image nudged elastic band method for finding saddle points and minimum energy paths. *J. Chem. Phys.* **113**, 9901–9904 (2000).

71. X. Wang, Y. Li, S. Wang, F. Zhou, P. Das, C. Sun, S. Zheng, Z.-S. Wu, 2D amorphous V_2O_5/graphene heterostructures for high-safety aqueous Zn-ion batteries with unprecedented capacity and ultrahigh rate capability. *Adv. Energy Mater.* **10**, 2000081 (2020).

72. Y. Ma, W. Cao, Y. Liu, Q. Li, S. Cai, S.-J. Bao, M. Xu, Amorphous vanadium oxides with dual ion storage mechanism for high-performance aqueous zinc ion batteries. *Small* **20**, e2306790 (2024).

73. B. Fei, Z. Liu, J. Fu, X. Guo, K. Li, C. Zhang, X. Yang, D. Cai, J. Liu, H. Zhan, In situ induced core-shell carbon-encapsulated amorphous vanadium oxide for ultra-long cycle life aqueous zinc-ion batteries. *Adv. Funct. Mater.* **33**, 2215170 (2023).

74. R. Wang, H. Dai, T. Zhang, J. Zhou, L. Yin, J. Zhou, G. Sun, Heterostructure design of amorphous vanadium oxides@carbon/graphene nanoplates boosts improved capacity, cycling stability and high rate performance for Zn^{2+} storage. *Adv. Funct. Mater.*, 2421857 (2024).

75. C. Hu, B. Li, K. Nie, Z. Wang, Y. Zhang, L. Yi, X. Hao, H. Zhang, S. Chong, Z. Liu, W. Huang, Ultrafast tailoring amorphous $Zn_{0.25}V_2O_5$ with precision-engineered artificial atomic-layer $1T'$-MoS_2 cathode electrolyte interphase for advanced aqueous zinc-ion batteries. *Angew. Chem. Int. Ed. Engl.* **64**, e202413173 (2025).

76. D. Jia, Z. Shen, Y. Lv, Z. Chen, H. Li, Y. Yu, J. Qiu, X. He, In situ electrochemical tuning of MIL-88B(V)@rGO into amorphous V_2O_5@rGO as cathode for high-performance aqueous zinc-ion battery. *Adv. Funct. Mater.* **34**, 2308319 (2023).

77. Z. Zhao, M. Liu, F. Liu, H. Jing, B. Xu, K. Song, W. Zhang, W. Zheng, Architecting V_2O_5 with a triune crystal water-amorphous-crystalline feature for robust zinc-ion batteries. *Nano Lett.* **24**, 13927–13934 (2024).

78. J. Guo, B. He, W. Gong, S. Xu, P. Xue, C. Li, Y. Sun, C. Wang, L. Wei, Q. Zhang, Q. Li, Emerging amorphous to crystalline conversion chemistry in Ca-doped VO_2 cathodes for high-capacity and long-term wearable aqueous zinc-ion batteries. *Adv. Mater.* **36**, e2303906 (2024).

79. F. Zhao, S. Gong, H. Xu, M. Li, L. Li, J. Qi, H. Wang, Z. Wang, Y. Hu, X. Fan, C. Li, J. Liu, In situ constructing amorphous V_2O_5@$Ti_3C_2T_x$ heterostructure for high-performance aqueous zinc-ion batteries. *J. Power Sources* **544**, 231883 (2022).

80. Y. Zhang, J. Qin, M. Batmunkh, W. Li, H. Fu, L. Wang, M. Al-Mamun, D. Qi, P. Liu, S. Zhang, Y. L. Zhong, Scalable spray drying production of amorphous V_2O_5-EGO 2D heterostructured xerogels for high-rate and high-capacity aqueous zinc ion batteries. *Small* **18**, e2105761 (2022).

81. X. Ma, X. Cao, M. Yao, L. Shan, X. Shi, G. Fang, A. Pan, B. Lu, J. Zhou, S. Liang, Organic-inorganic hybrid cathode with dual energy-storage mechanism for ultrahigh-rate and ultralong-life aqueous zinc-ion batteries. *Adv. Mater.* **34**, e2105452 (2022).

82. P. He, G. Zhang, X. Liao, M. Yan, X. Xu, Q. An, J. Liu, L. Mai, Sodium ion stabilized vanadium oxide nanowire cathode for high-performance zinc-ion battery. *Adv. Energy Mater.* **8**, 1702463 (2018).

83. Y. Yang, Y. Tang, S. Liang, Z. Wu, G. Fang, X. Cao, C. Wang, T. Lin, A. Pan, J. Zhou, Transition metal ion-preintercalated V_2O_5 as high-performance aqueous zinc-ion battery cathode with broad temperature adaptability. *Nano Energy* **61**, 617–625 (2019).

84. C. Xia, J. Guo, P. Li, X. Zhang, H. N. Alshareef, Highly stable aqueous zinc-ion storage using a layered calcium vanadium oxide bronze cathode. *Angew. Chem. Int. Ed. Engl.* **57**, 3943–3948 (2018).

85. Y. Yang, Y. Tang, G. Fang, L. Shan, J. Guo, W. Zhang, C. Wang, L. Wang, J. Zhou, S. Liang, Li^+ intercalated V_2O_5·nH_2O with enlarged layer spacing and fast ion diffusion as an aqueous zinc-ion battery cathode. *Energ. Environ. Sci.* **11**, 3157–3162 (2018).

86. S. Liu, H. Zhu, B. Zhang, G. Li, H. Zhu, Y. Ren, H. Geng, Y. Yang, Q. Liu, C. C. Li, Tuning the kinetics of zinc-ion insertion/extraction in V_2O_5 by in situ polyaniline intercalation enables improved aqueous zinc-ion storage performance. *Adv. Mater.* **32**, e2001113 (2020).

87. N. Liu, X. Wu, L. Fan, S. Gong, Z. Guo, A. Chen, C. Zhao, Y. Mao, N. Zhang, K. Sun, Intercalation pseudocapacitive Zn^{2+} storage with hydrated vanadium dioxide toward ultrahigh rate performance. *Adv. Mater.* **32**, e1908420 (2020).

88. J. Kim, S. H. Lee, C. Park, H. S. Kim, J. H. Park, K. Y. Chung, H. Ahn, Controlling vanadate nanofiber interlayer via intercalation with conducting polymers: Cathode material design for rechargeable aqueous zinc ion batteries. *Adv. Funct. Mater.* **31**, 2100005 (2021).

89. S. Chen, K. Li, K. S. Hui, J. Zhang, Regulation of lamellar structure of vanadium oxide via polyaniline intercalation for high-performance aqueous zinc-ion battery. *Adv. Funct. Mater.* **30**, 2003890 (2020).